Energy 345 (2026) 140108

Contents lists available at ScienceDirect

Energy

journal homepage: www.elsevier.com/locate/energy

Bridging molecular modeling and 3E cycle analysis in absorption cooling using biomass-based solvents

Isaías Huenuvil-Pacheco [a,b], Miguel Viar [c], Gabriel Zarca [c], Ane Urtiaga [c], Andrés Mejía [a], Fèlix Llovell [b,*]

[a] Departamento de Ingeniería Química, Universidad de Concepción, POB 160 - C, 4070386, Concepción, Biobío, Chile
[b] Department of Chemical Engineering, ETSEQ, Universitat Rovira i Virgili, Avda Països Catalans 26, 43007 Tarragona, Spain
[c] Department of Chemical and Biomolecular Engineering, Universidad de Cantabria, Av. Los Castros 46, 39005 Santander, Spain

ARTICLE INFO

Keywords:
SAFT-VR Mie EoS
Biomass-based solvents
Fluorinated refrigerants
Absorption refrigeration
3E analysis
Indirect emissions

ABSTRACT

Improving the sustainability of thermal processes has fostered growing interest in renewable, biodegradable, and non-toxic compounds. Among them, biomass-derived solvents present significant advantages over traditional petroleum-based alternatives, contributing to circular economy strategies. In this study, we develop a comprehensive thermodynamic framework to assess the potential of new refrigerant–solvent working pairs for absorption refrigeration systems (ARS). These pairs combine fluorinated refrigerants and CO_2 with five green organic solvents: Propylene Carbonate, Solketal, Terpinolene, γ-Valerolactone, and Rhodiasolv PolarClean. The solubility of refrigerants in these solvents is modeled using an extended version of the SAFT-VR Mie equation of state, incorporating descriptors for planar ring structures and polar contributions. Refrigerants are treated as non-associating but dipolar fluids, and their thermophysical properties are successfully reproduced. Mixture behavior is captured with a single, temperature-independent binary interaction parameter, enabling reliable extrapolation to process conditions. The validated model is employed to quantify the working capacity of each refrigerant–solvent pair, serving as a pre-screening tool to choose the most promising pairs for cycle simulation. Single-effect (SE) and compression-assisted (CA) ARSs are evaluated through a detailed parametric study. Then, a comprehensive 3E analysis (energetic, exergetic, and environmental) is conducted, incorporating Key Performance Indicators, including the energy and exergy coefficients of performance, circulation ratio, high-pressure levels, and the total equivalent warming impact (TEWI). Finally, the TOPSIS multi-criteria decision-making method is applied to rank the working pairs and identify the best options for each configuration, revealing that R32/γ-Valerolactone stands out as the best working pair in CA-Cycles when environmental concerns are considered.

1. Introduction

In the context of an increasing energy demand and the urgent need to reduce greenhouse gas emissions, most efforts are devoted to accelerate the transition to renewable energy and reduce reliance on fossil fuels [1]. In this framework, the development of sustainable refrigeration technologies has become a critical priority. Among different options, Absorption Refrigeration Systems (ARSs) offer a sustainable alternative to conventional vapor-compression refrigeration cycles (VCRCs), particularly when waste heat or renewable energy sources are available. In fact, some studies highlight that ARSs offer significantly higher energy efficiency than conventional VCRCs with building-integrated applications, expecting to cut energy consumption by as much as 44% [2]. However, a key factor in the performance and feasibility of these systems is the selection of an appropriate working pair: a refrigerant and absorbent combination with high energy efficiency, low environmental impact, and favorable thermophysical properties.

Traditionally, working pairs such as H_2O–NH_3 and LiBr–H_2O have dominated the field, being potentially used in most applications. However, they present well-known drawbacks. The LiBr–H_2O pair is prone to crystallization and corrosion, which can shorten the lifespan of the equipment [3,4], while the H_2O–NH_3 system demands a rectification step after desorption due to the challenging separation process, apart from the safety concerns in case of an accidental release of ammonia [5]. Consequently, there is a very active field of research related to the proposal of new working pairs able to overcome these disadvantages, while maintaining a good technical performance. Indeed, a wide

* Corresponding author.
E-mail address: felix.llovell@urv.cat (F. Llovell).

https://doi.org/10.1016/j.energy.2026.140108
Received 9 September 2025; Received in revised form 30 December 2025; Accepted 18 January 2026
Available online 19 January 2026
0360-5442/© 2026 The Authors. Published by Elsevier Ltd. This is an open access article under the CC BY license (http://creativecommons.org/licenses/by/4.0/).

variety of fluids from multiple organic and inorganic families have been studied as potential refrigerants, being combined with a vast number of possible solvents. The reader is referred to several reviews on the topic for further details [5–7].

The choice of optimal absorbent–refrigerant pairs requires accurate prediction of the thermophysical properties of both compounds under diverse operating conditions. Reliable data on properties such as vapor–liquid equilibrium, enthalpy, entropy, viscosity, and thermal conductivity are essential to optimize system design and ensure operational safety and efficiency. This can be achieved through a systematic experimental evaluation. However, this task may become cumbersome if a wide variety of combinations are possible. In this regard, the use of computational tools based on accurate and predictive thermodynamic models becomes extremely useful for a pre-selection of the best candidates. As such, the dual challenge of discovering advanced working pairs and modeling their behavior with high fidelity remains a key focus in current research on absorption refrigeration technologies [3,5,8].

Owing to their favorable thermophysical and environmental characteristics, absorption refrigeration studies have extensively investigated hydrofluorocarbons (HFCs), hydrofluoroolefins (HFOs), and carbon dioxide (CO_2) as refrigerants, provided that a suitable absorbent is available. In this context, recent research has turned to explore ionic liquids (ILs) as potential absorbents, due to their negligible vapor pressure and the possibility of tailoring their physicochemical properties. Kim et al. [9] carried out one of the earliest thermodynamic assessments of ARSs based on HFCs-IL mixtures, highlighting the potential of imidazolium-based ILs as alternative absorbents driven by low-grade waste heat. Wu and co-workers published a series of three papers [10–12] where they explored the performance of HFOs in combination with ILs using the NRTL activity coefficient model, and highlighted the potential of these systems to improve energy efficiency and reduce environmental impact in absorption refrigeration. Also with NRTL, Asensio-Delgado et al. [13] evaluated 16 F-gas/IL pairs for ARSs, focusing on low-GWP HFCs and HFOs in single-effect (SE) and compression-assisted (CA) cycles, achieving the best efficiency using R32–[C_2mim][Tf_2N]. Huang et al. [14] proposed a CA absorption refrigeration–heating system applied to liquid-cooled data centers, employing working pairs such as R152a–[C_6mim][Tf_2N]. Their results demonstrated that the inclusion of an auxiliary compressor significantly extends the operational window of absorption systems, enabling simultaneous refrigeration, and heating and improving overall energetic and exergetic performance under low-temperature driving conditions. While all these studies provide valuable information, the selection of the working pair is, in most cases, based on predefined candidates and property correlations, without a molecular-level thermodynamic foundation or a systematic environmental comparison across alternative refrigerant–absorbent combinations. In addition to the use of correlations and activity coefficient models, Zhang and coworkers [15] employed Artificial Neural Networks (ANNs) based on COSMO-RS calculations to screen a big database of 12080 ILs and 6 HFCs or HFOs for ARS applications, suggesting the pair R152a–[C_3M_5GU][DMP] as the best option. More recently, Chu et al. [16] have also applied machine learning algorithms to find optimal HFC–HFO with IL pairs using an atomic scale model, suggesting that the combination of OMIM cation-based ILs and R218 are suitable for a wide range of conditions. Regarding the use of CO_2, CA cycles based on CO_2–IL mixtures have been explored as a strategy to alleviate the high operating pressures of conventional CO_2 vapor compression systems. Li et al. [17] investigated several compression–absorption configurations using CO_2–[C_2mim][Tf_2N] as the working pair, showing that the integration of an absorbent loop can significantly reduce the high-side pressure while maintaining a competitive refrigeration performance. Apart from the energetic efficiency, a common concern remains regarding the use of ILs, especially due to their high viscosity, substantial cost, and, in some cases, environmental issues associated with their synthesis, limited biodegradability, and potential toxicity [18].

In the search for alternative solvents that can compete with ILs, but have an improved sustainability profile, several families of compounds have received attention. From the one hand, Deep Eutectic Solvents (DESs) are often regarded as IL-type systems; however, they are distinct by definition, as they consist of mixtures of two or more components whose melting point is significantly lower than that predicted for an ideal mixture of the same constituents [19]. DESs are characterized by an easy synthesis, low cost, and low environmental concern if the appropriate compounds are selected. In a series of pioneering contributions, Abedin et al. [20,21] used COSMO-RS and molecular simulations to evaluate R134a, R245fa, R1234ze(E) and HFO1336mzz with several DESs based on Choline Chloride and Ethylenglycol (ethaline) or Levulinic Acid as working pairs for ARSs, with R245fa-ethaline showing the highest performance. Haghbakhsh and coworkers [22] performed and energetic and exergetic analysis of the potential use of ethaline, reline and glyceline DESs, using ammonia as a classical refrigerant in ARS, by modeling the system combining the SRK equation of state with the NRTL approach. In this study, they corroborated a better performance of Ethylenglycol-based DESs. More recently, Imas et al. [23] employed the PC-SAFT equation of state to evaluate the performance of absorption refrigeration cycles using various HFC refrigerants with DESs as absorbents. Their analysis showed that only a subset of refrigerant–DES pairs are thermodynamically viable, with IL-based DESs combined with R227ea or R236ea offering the highest coefficient of performance.

From the other hand, the use of fluorinated refrigerants with organic solvents as working pairs for ARSs has also been explored in recent contributions from both thermodynamic and system-design perspectives. Kong et al. [8] performed a large-scale screening of more than sixty low-GWP refrigerant/organic solvent combinations, including some HFOs, using the UNIFAC-DMD model and correlating excess thermodynamic properties with cycle performance indicators in SE absorption systems. Their work highlighted the importance of molecular polarity and intermolecular interactions in the working pair selection, providing valuable guidelines for preliminary screening. In a different work, Zhang et al. [2] proposed a systematic methodology based on pinch technology to optimize internal heat recovery and system configurations using fluorinated refrigerants with organic solvents in both SE and CA-ARSs, demonstrating that appropriate heat-integration strategies can substantially enhance the coefficient of performance and broaden operating ranges. Finally, there is a growing interest in biobased-derived organic solvents as absorbents. These compounds are renewable, biodegradable and non-toxic, and contribute to circular economy strategies by utilizing agricultural and forestry residues. Their application spans green synthesis, cleaning products, polymer processing, and gas absorption, offering an attractive alternative to petroleum-based solvents. In a previous contribution [24], new measurements of the solubility of several HFCs and HFOs in five green solvents, Solketal (2,2 – dimethyl – 1,3 – dioxolane – 4-methanol), Terpinolene, γ-Valerolactone, Rhodiasolv Polarclean (methyl 5-(dimethylamino) – 2$^-$ methyl – 5-oxopentanoate) and Propylene Carbonate, were presented and modeled using the NRTL approach, being tested for the first time as potential working pairs in ARS cycles. The results obtained highlighted that R32 pairs show competitive results, while R1234ze(E) may represent a low-GWP alternative of analogous flammability, as both are classified as lower flammability refrigerants (safety class A2L). However, that study did not explore a detailed parametric analysis of the key operating variables governing cycle performance, nor did it assess the environmental implications associated with direct and indirect refrigerant emissions. More broadly, although existing contributions in literature constitute important advances, absorption refrigeration studies mostly rely on activity-coefficient thermodynamic models and tend to address working-pair screening, cycle configuration, or performance assessment in a fragmented manner. In most cases, energetic or

exergetic indicators are evaluated in isolation, without a systematic integration of environmental metrics or a consistent comparison between SE and CA configurations. As a consequence, the fundamental advantages and trade-offs of alternative working pairs are often dispersed across different studies, hindering the establishment of a clear and rational hierarchy among competing options. A common framework capable of consistently linking molecular-level thermodynamics with cycle-level energy, exergy, and environmental performance is therefore still lacking.

In this work, we explicitly address these limitations by implementing a unified molecular-to-process framework based on the Statistical Associating Fluid Theory with a Mie intermolecular potential (SAFT-VR Mie) [25], enabling a consistent assessment of working-pair selection, ARS cycle performance, and environmental impact within a single methodology. For this purpose, new accurate molecular models, including all possible physical effects, caused by hydrogen bonding, polarity and branched/ring structures, have been proposed to estimate the pure thermodynamic properties of a selection of biomass-derived solvents with high accuracy. A similar approach is followed for the refrigerants, including five F-gases and CO_2. Building on this foundation, the thermodynamic framework allows a detailed parametric analysis of all the operational variables of SE and CA-ARSs. A complete 3E (energy, exergy and environmental) analysis is carried out, with focus on the efficient use of energy and the determination of a series of Key Performance Indicators (KPIs). Specifically, the Energy and Exergy Coefficient of Performance (COP and ECOP, respectively) for selected working pairs are studied under representative operating conditions. In addition, an estimation of the environmental impact is carried out through the adaptation of the Total Warming Environmental Impact (TEWI) methodology to ARS cycles. The different KPIs are leveraged and fairly compared using the Technique for Order of Preference by Similarity to Ideal Solution (TOPSIS) statistical methodology, allowing to identify the most promising combinations. This holistic approach provides both molecular-level insight and system-level guidance for the design of next-generation absorption refrigeration systems with low environmental impact and high efficiency.

2. Theory

2.1. Molecular-based equation of state: SAFT-VR Mie

The theoretical model employed to describe all the thermophysical properties of the systems involved in this work is the molecular-based SAFT-VR Mie equation of state (EoS), a variant of the original SAFT equation [26]. As any SAFT-type equation, it is expressed in terms of the Helmholtz energy, A, as a sum of the following microscopic contributions:

$$\frac{A}{Nk_BT} = \frac{A^{ig}}{Nk_BT} + \frac{A^{mono}}{Nk_BT} + \frac{A^{chain}}{Nk_BT} + \frac{A^{assoc}}{Nk_BT} + \frac{A^{pol}}{Nk_BT} \tag{1}$$

where N is the Avogadro constant, k_B is the Boltzmann constant and T is the absolute temperature. The different superscripts refer to the ideal gas term, A^{ig}, the monomer segment interactions, A^{mono}, the molecular chain formation, A^{chain}, the intermolecular association to account for strongly directional intermolecular interactions such as hydrogen bonds, A^{assoc}, and the effect of the presence of permanent dipolar moments, A^{pol} [25,27,28].

For the particular case of cyclic or branched molecules, the conventional chain contribution, A^{chain}, is replaced by the ring term, A^{ring}, which explicitly accounts for the non-linear molecular structure [29]. The ring contribution is defined as follows:

$$\frac{A^{ring}}{Nk_BT} = -\left(m_s - 1 + \chi\eta\right)\ln\left[g^{\mathrm{Mie}}(\sigma)\right] \tag{2}$$

where η is the packing fraction, and χ is a geometric parameter that depends on the molecular topology and the reference potential. The value of m_s corresponds to the number of segments used to represent the molecular structure and is selected to reflect the most representative geometry. Note that for non-cyclic or non-branched compounds, the geometric parameter becomes zero and the equation reduces to the classical chain term.

SAFT-VR Mie uses a Mie intermolecular potential to describe the interactions among the monomers, A^{mono}. The potential is characterized by the effective segment diameter (σ), the dispersive energy describing the strength of interaction (ε/k_B), and the repulsive (λ_r) and attractive (λ_a) exponents. While λ_a is always fixed at 6, λ_r is a parameter fitted to each molecule. Non-associating and non-polar fluids are then characterized by 4 parameters, the segment number (m_s), coming from the chain term, and the σ, ε/k_B and λ_r Mie parameters. If association is present, the site–site interaction energy (ε^{AB}) and the association range (r_c^{AB}) are added. Moreover, the association scheme must be defined, either using the original Huang and Radosz framework [30] or in a compact form based on three numbers: the number of bipolar, B, positive, P, and negative, N, sites [31]. Finally, in case polarity is significant in the fluid, the dipolar moment (μ_{pol}) and the number of polar segments (n_{pol}) are also included in the model.

The application of the SAFT-VR Mie EoS to mixtures is straightforward. However, it is crucial to account for cross-interactions between unlike components through the use of one energy binary interaction parameter. The unlike intermolecular parameters, namely the repulsive and attractive exponents λ_{ij}, the size parameter σ_{ij}, and the dispersion energy ε_{ij}, are determined using the following combining rules:

$$\left(\lambda_{ij} - 3\right) = \sqrt{\left(\lambda_{ii} - 3\right)\left(\lambda_{jj} - 3\right)} \tag{3}$$

$$\sigma_{ij} = \frac{(\sigma_{ii} + \sigma_{jj})}{2} \tag{4}$$

$$\varepsilon_{ij} = \sqrt{\varepsilon_{ii}\varepsilon_{jj}}\frac{\sqrt{\left(\sigma_{ii}\sigma_{jj}\right)^3}}{\sigma_{ij}^3}(1 - k_{ij}) \tag{5}$$

Here, k_{ij} is a binary interaction parameter obtained by fitting to experimental vapor–liquid equilibrium (VLE) data for the absorption of the binary systems. This parameter was determined by minimizing the following objective function:

$$\mathrm{OF}\,(k_{ij}) = w_x \sum_{j=1}^{n}\left[\sum_{i=1}^{2}\left(x_{i,j}^{cal} - x_{i,j}^{exp}\right)^2\right] + w_p \sum_{j=1}^{n}\left[\frac{P_j^{cal} - P_j^{exp}}{P_j^{exp}}\right] \tag{6}$$

For dew point calculations, n denotes the number of experimental data points, x_i is the liquid-phase mole fraction of component i, and P is the dew pressure. The superscripts *cal* and *exp* represent the calculated and experimental values, respectively. The weighting factors for the liquid composition and dew pressure errors are denoted by w_x and w_P, respectively.

Phase equilibrium calculations are solved by imposing the classical equilibrium conditions of equality of temperature, pressure and chemical potential of each compound in each phase. Once solved, it is possible to describe any thermodynamic property. For the particular case of ARSs, it is necessary to evaluate the enthalpy of the different streams. The total enthalpy of pure compounds, H_i, is calculated from the EoS as the sum of the reference, ideal and residual contributions,

$$H_i = H^{ref} + H^{ideal} + H^{res} \tag{7}$$

where H^{ref} is the enthalpy at an arbitrary fixed reference state, T^{ref} = 298.15 K. The ideal contribution to the enthalpy, H_i^{id}, is calculated by integrating the ideal-gas isobaric heat capacity, C_p^{id}, over temperature from the reference state to the temperature of interest T,

$$H_i^{id} = \int_{T^{ref}}^{T} C_p^{id}\,dT \tag{8}$$

C_p^{id} is represented as a polynomial function of temperature:

$$C_p^{id} = a + bT + cT^2 + dT^3 \tag{9}$$

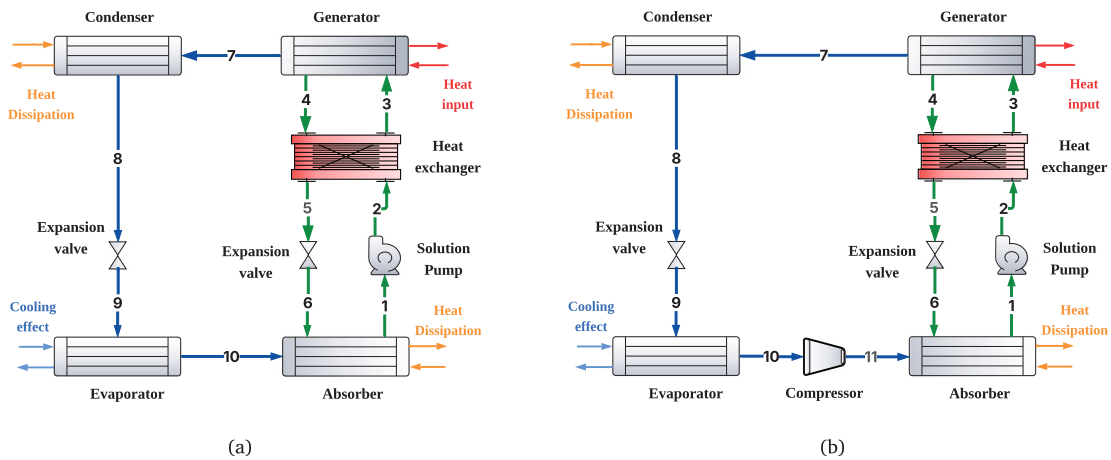

Fig. 1. Schematic diagram of (a) SE-ARS and (b) CA-ARS. Each stream is numbered to facilitate understanding of the energy balances described in the text.

where the coefficients a, b, c, and d were taken from literature [32] for the refrigerants, while being fitted from heat capacity data following previous work [24] for the case of solvents.

H^{res} is the residual enthalpy of pure components obtained from SAFT-VR Mie using the following expression,

$$\frac{H^{res}}{Nk_BT} = \frac{A^{res}}{Nk_BT} - \frac{1}{Nk_B}\left(\frac{\partial A^{res}}{\partial T}\right) + Z - 1 \tag{10}$$

For binary mixtures, the total molar enthalpy (H_{mix}) was calculated as

$$H_{\text{mix}} = x_1 H_1^{id} + (1 - x_1) H_2^{id} + H_{\text{mix}}^{\text{res}} \tag{11}$$

where the term $H_{\text{mix}}^{\text{res}}$ corresponds to the residual enthalpy of the mixture, accounting for non-ideal interactions, and was evaluated using the EoS with the open source code SGTPy [33].

2.2. Modeling of absorption cooling cycles

Absorption refrigeration cycles were simulated considering two configurations: (1) a single-effect absorption refrigeration system (SE-ARS) and (2) a compression-assisted hybrid absorption refrigeration system (CA-ARS). A schematic image for both diagrams can be seen in Fig. 1. In the SE-ARS, the liquid mixture of refrigerant and solvent is pressurized and sent to the generator, where thermal energy, preferably from waste heat or renewable sources, is used to separate the refrigerant. The vapor is then condensed at high pressure, expanded, and introduced into the evaporator to absorb heat and produce the desired cooling effect. The refrigerant is subsequently reabsorbed by the solvent, completing the cycle. In the CA-ARS, a small compressor is placed before the absorber to increase the refrigerant pressure by means of a certain Compression Ratio (CR), $p_a = p_e \cdot \text{CR}$, with the purpose to enhance its solubility in the solvent. All simulations were carried out using an own-made `Python` program with all thermodynamic properties calculated through SAFT-VR Mie. The simulations were conducted under the following set of assumptions, based on previous literature sources [10,11,24]:

1. Both systems operate under steady-state conditions.
2. Thermodynamic equilibrium is assumed for the streams exiting the absorber and generator. Consequently, mass-transfer limitations are neglected, considering the low viscosity of all solvents studied (see details in Section 2.3).
3. Heat losses to the environment, pressure drops and flow resistances are neglected.
4. Expansion valves are modeled as ideal isenthalpic devices.
5. All working fluids are assumed to be in saturated liquid or vapor states.
6. The solution heat exchanger is modeled with a fixed effectiveness of 0.8.
7. In accordance with ASHRAE guidelines, the outlet temperature of the generator is assumed equal to its inlet temperature.
8. For the CA-ARS configuration, the compressor is assumed to operate under isentropic conditions, with a mechanical efficiency set to 0.7.

The cycle operates at two distinct pressure levels, which are determined from the saturation pressure of the pure refrigerant. The low-pressure level corresponds to the evaporator temperature, $P_{\text{low}} = P_{\text{refr}}^{\text{sat}}(T_e)$, while the high-pressure level is defined at the condenser temperature, $P_{\text{high}} = P_{\text{refr}}^{\text{sat}}(T_{\text{cond}})$. Streams 1, 6, 9 and 10 operate at the low-pressure level (P_{low}), whereas the remaining streams operate at the high-pressure level (P_{high}). The only exception is stream 11 (in the CA-ARS), which operates at $P_{\text{low}} \cdot \text{CR}$.

The following balance equations are expressed in terms of the circulation factor, f, which is defined as the ratio between the mass flow rate of the dilute solution leaving the absorber ($\dot{m}_{dil}$) and the mass flow rate of refrigerant entering the evaporator ($\dot{m}_r$).

$$f = \frac{\dot{m}_{dil}}{\dot{m}_r} = \frac{1 - w_{con}}{\Delta w} = \frac{1 - w_{con}}{w_{dil} - w_{con}} \tag{12}$$

Absorption cycles were simulated by applying mass and energy balances according to the scheme shown in Fig. 1. The energy balance for the generator can be written as:

$$Q_g + \dot{m}_0 \cdot h_3 \cdot f = \dot{m}_0 \cdot h_7 + \dot{m}_0 \cdot h_4 \cdot (f - 1) \tag{13}$$

where $\dot{m}_0$ denotes the refrigerant mass flow rate, and h_i represents the specific enthalpy of the ith stream. The mass flow rate is fixed at 1 kg s^{-1}. The remaining devices within the system are described by means of energy balances, which are presented below:

$$Q_e + \dot{m}_0 \cdot h_9 = \dot{m}_0 \cdot h_{10} \tag{14}$$

$$Q_a + \dot{m}_0 \cdot h_1 \cdot f = \dot{m}_0 \cdot h_6 \cdot (f - 1) + \dot{m}_0 \cdot h_{10} \tag{15}$$

$$Q_c + \dot{m}_0 \cdot h_8 = \dot{m}_0 \cdot h_7 \tag{16}$$

$$Q_x = \dot{m}_0 \cdot (h_3 - h_2) \cdot f = \dot{m}_0 \cdot (h_4 - h_5) \cdot (f - 1) \tag{17}$$

Here, Q_e is the heat extracted by the evaporator, Q_a is the heat released in the absorber, Q_c is the heat rejected in the condenser, and Q_x is the heat exchanged in the solution heat exchanger. For the latter, it is assumed to operate with an heat exchanger efficiency η_x, which is expressed as follows:

$$\eta_x = \frac{T_4 - T_5}{T_4 - T_1} \tag{18}$$

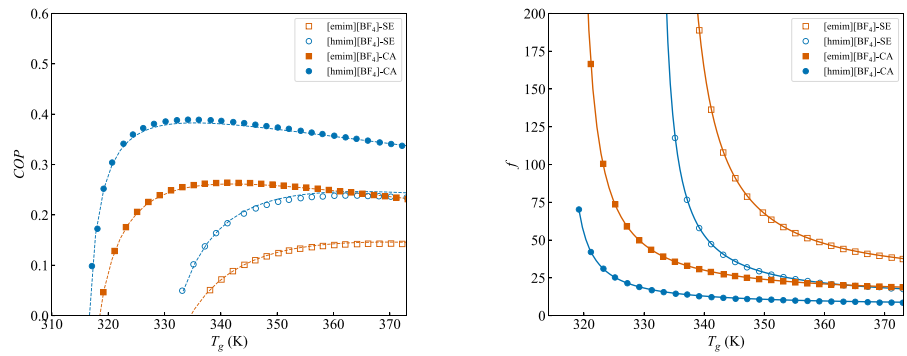

(a) (b)

Fig. 2. Model verification of absorption refrigeration cycles for R1234ze(E) + $[C_2mim][BF_4]$ (orange) and R1234ze(E) + $[C_6mim][BF_4]$ (blue). (a) COP as a function of the generator temperature (b) Circulation ratio, f, as a function of the generator temperature. Symbols represent the results from Wu et al. [11], and lines the calculations performed with our `Python` code.

The outlet enthalpy of the pumped solution is calculated using:

$$h_2 = h_1 + \frac{W_p}{\dot{m}_0 \cdot f} \tag{19}$$

The pump work, W_p, is typically negligible in comparison to the system's cooling capacity [34]. As expansion valves are assumed isenthalpic, no change in enthalpy is considered across them:

$$h_9 = h_8 \qquad h_6 = h_5 \tag{20}$$

When moving to CA-ARS, the pressure of the inlet stream to the absorber p_a is calculated using a compression ratio (CR) that multiplies the evaporator pressure (p_e)

$$p_a = p_e \cdot CR \tag{21}$$

The energy balance is modified due to the addition of the stream following compression. The revised energy balance is expressed as follows:

$$Q_a + \dot{m}_0 \cdot h_1 \cdot f = \dot{m}_0 \cdot h_{11} + \dot{m}_0 \cdot h_6 \cdot (f - 1) \tag{22}$$

The compressor work is evaluated between the outlet of the evaporator and the inlet of the condenser as:

$$W_{\text{comp}} = \frac{\dot{m}_0 (h_{11} - h_{10})}{\eta_{\text{comp}}} \tag{23}$$

where η_{comp} is the mechanical efficiency of the compressor.

To evaluate the performance of the proposed working pairs, a series of Key Performance Indicators (KPIs) were selected. The energetic coefficient of performance (COP) of the cycles is defined as the ratio between the cooling capacity delivered by the evaporator and the energy required by the system. For SE-ARS, this corresponds to the thermal energy input required by the generator, while for the CA-ARS case, it is necessary to add the compressor work:

$$COP_{SE} = \frac{Q_e}{Q_g} \quad ; \quad COP_{CA} = \frac{Q_e}{Q_g + W_{\text{comp}}} \tag{24}$$

Additionally, the exergy coefficient of performance (ECOP) for the SE-ARS and CA-ARS are given, respectively, by:

$$ECOP_{SE} = \frac{Q_e \left|1 - \frac{T_{\text{ref}}}{T_e}\right|}{Q_g \left(1 - \frac{T_{\text{ref}}}{T_g}\right)} \quad ; \quad ECOP_{CA} = \frac{Q_e \left|1 - \frac{T_{\text{ref}}}{T_e}\right|}{Q_g \left(1 - \frac{T_{\text{ref}}}{T_g}\right) + W_{\text{comp}}} \tag{25}$$

where T_{ref} is the reference environment temperature used for exergy analysis, which in this work is set to 298.15 K.

2.3. Model validation

To assess the reliability of the proposed thermodynamic and cycle models, two different validations were carried out. Firstly, the `Python` code developed in this work was validated by reproducing the results reported by Wu et al. [11] for R1234ze(E) with two ionic liquids, $[C_2mim][BF_4]$ and $[C_6mim][BF_4]$ considering both, SE−ARS and CA−ARS. In this case, the NRTL activity coefficient thermodynamic model was employed using the interaction parameters provided by the authors. Fig. 2 presents the COP and the circulation ratio, f, where the symbols correspond to the literature data and the lines represent the results obtained with our cycle model, showing perfect agreement over the entire range evaluated.

Secondly, the thermodynamic model employed in the present work was validated against the results of a single-stage absorption refrigeration system reported by Herold et al. in Example 9.2 [34], using the classical working pair NH_3–H_2O. This system was selected as it represents a benchmark pair in absorption refrigeration studies. All thermophysical properties, saturated pressures, solubility and residual enthalpies, were calculated using the SAFT-VR Mie equation of state. Further details on the pure-component (Figure S.1), mixture models (Figure S.2) and calculation details are provided in Supplementary Material (Section S.1). The results obtained in this study, summarized in Table 1, show good agreement with the published data, with deviations of 5.69% in the coefficient of performance and 2.75% in the circulation ratio. In addition, SAFT-VR Mie shows a good performance in describing the operating pressure levels (low and high pressures) and the solubility of the binary mixture.

2.4. Environmental analysis

Apart from the classical energy and exergy analysis, a study of the total emissions of the system, associated to the refrigerants and cycle choice, is carried out through the calculation of the Total Equivalent Warming Impact (TEWI) [35]. TEWI is a metric commonly used to assess the environmental impact of refrigerants throughout the operational lifetime of a cooling system. TEWI accounts for both direct greenhouse gas (GHG) emissions, arising from refrigerant leakage and end-of-life disposal, and indirect emissions, related to the energy consumed during operation. Although the TEWI metric is primarily designed for vapor-compression refrigeration systems (VCRCs), it can also be applied to ARSs. However, it must be noted that in SE-ARSs, the indirect emissions are limited to the work caused by the pump, which is typically negligible. In CA-ARSs, the refrigerant is subject to leakage and disposal risks similar to those in VCRCs, particularly when

Table 1
Comparison of the present model predictions for the NH_3–H_2O system with the results reported by Herold et al. [34]. The operating conditions are T_{evap} = 263.15 K, T_{abs} = 313.15 K, and T_{cond} = 313.15 K. Thermophysical properties of the NH_3–H_2O mixture were evaluated using the SAFT-VR Mie equation of state.

Performance parameter	Present work	Herold et al.	% deviation
Concentration of strong solution (x_{con}, kg/kg)	0.377	0.396	4.89
Concentration of weak solution (x_{dil}, kg/kg)	0.277	0.296	6.54
Coefficient of Performance, COP	0.472	0.447	5.69
Circulation ratio, f	7.23	7.03	2.75
Low pressure (kPa)	291.75	286.40	1.87
High pressure (kPa)	1544.26	1556.00	0.75

fluorinated refrigerants are used. Moreover, the indirect emissions include both thermal and mechanical energy inputs. By adapting the energy consumption term (E_a) to reflect the hybrid nature of CA-ARS operation, where mechanical compression aids the thermal desorption process, TEWI remains a suitable tool for quantifying the overall climate impact of these systems. This enables a consistent comparison across conventional and alternative cooling technologies under the same environmental assessment framework.

The total TEWI is expressed as:

$$\text{TEWI} = \underbrace{\text{GWP} \cdot (L \cdot m \cdot n + m \cdot (1-\alpha))}_{\text{Direct}} + \underbrace{E_a \cdot \beta \cdot n}_{\text{Indirect}} \tag{26}$$

Here, L is the annual leakage rate, m is the initial refrigerant charge, n is the system lifetime in years, and α is the recovery or recycling factor at end-of-life. The coefficient β is the country-dependent indirect emission factor. The indirect term, E_a, represents the annual energy consumption of the system and can be defined as:

$$E_a = \omega_{\text{comp}} \cdot \dot{m}_{\text{ref}} \cdot \text{AOT} \tag{27}$$

where ω_{comp} is the compressor's specific work, $\dot{m}_{\text{ref}}$ is the refrigerant mass flow rate, and AOT is the annual operating time in hours.

In the present study, a leakage rate of 1% is assumed for the SE-ARS, which is typically hermetically sealed and does not involve dynamic mechanical components. In contrast, a leakage rate of 3% is retained for the CA-ARS, where the presence of a compressor introduces additional leakage pathways associated with dynamic seals. This later percentage is in the low range of standard values in VCRC systems [36] as the work in the compressor is also less intensive [37]. The system is standardized to 10 years of lifetime. The recovery factor is taken as 0.70, following the AIRAH guidelines for refrigerant charges below 100 kg [35]. The emission factor β corresponding to the EU-27 electricity mix is used, with a value of 0.2839 kg CO_2–eq· kWh^{-1} [38], to evaluate the indirect environmental impact, thus reflecting the average carbon intensity of electricity generation within the European Union.

2.5. TOPSIS methodology

The Technique for Order of Preference by Similarity to Ideal Solution (TOPSIS) is a multi-criteria decision-making approach used to rank and select different alternatives [39] and is employed in this work to evaluate the best working pair. The methodology is applied by first normalizing the selected KPIs of the system (i.e. the decision matrix) according to Eq. (28):

$$r_{ij} = \frac{y_{ij}}{\sqrt{\sum_{k=1}^{m} y_{kj}^2}} \tag{28}$$

where y_{ij} is the value of the evaluated ith alternative KPI on the jth criterion, and r_{ij} is the normalized value. Then, it is necessary to decide on the weights given to each KPI:

$$v_{ij} = w_j^{(F)} \cdot r_{ij} \tag{29}$$

where v_{ij} is the weighted normalized value and $w_j^{(F)}$ is the weight of the jth criterion. A hybrid weighting methodology has been employed to estimate the relative importance of the different indicators. This approach combines an expert-based qualitative assessment of the relative importance of each indicator, denoted as $w_j^{(S)}$, with a quantitative statistical treatment of the variability observed in the dataset based on the entropy weight method (EWM), denoted as $w_j^{(O)}$ [40]. Details of the EWM procedure are provided in Section S2 of the Supplementary Material. The final weights are calculated as a convex combination of both contributions:

$$w_j^{(F)} = \beta\, w_j^{(S)} + (1-\beta)\, w_j^{(O)}, \tag{30}$$

where β = 0.75. This hybrid formulation preserves the physical relevance of the indicators through expert judgment, while simultaneously incorporating objective statistical information, thereby reducing the overall subjectivity of the weighting process.

Once this is done, the ideal (A^+) and anti-ideal (A^-) solutions for each criterion are calculated as:

$$A_j^+ = \begin{cases} \max_i v_{ij} & \text{if } j \in \text{benefit criterion} \\ \min_i v_{ij} & \text{if } j \in \text{cost criterion} \end{cases} \tag{31}$$

$$A_j^- = \begin{cases} \min_i v_{ij} & \text{if } j \in \text{benefit criterion} \\ \max_i v_{ij} & \text{if } j \in \text{cost criterion} \end{cases} \tag{32}$$

Then, the Euclidean distance from the ideal and anti-ideal solutions are computed and the relative closeness to the ideal solution is calculated:

$$S_i^+ = \sqrt{\sum_{j=1}^{n} (v_{ij} - A_j^+)^2}; \qquad S_i^- = \sqrt{\sum_{j=1}^{n} (v_{ij} - A_j^-)^2}; \tag{33}$$

Finally, the P_i score, calculated through Eq. (34), allows to establish a ranking of values, where higher values indicate better overall performance.

$$P_i = \frac{S_i^-}{S_i^+ + S_i^-} \tag{34}$$

3. Engineering applicability of selected solvents

In this work, we selected five organic solvents to evaluate their performance in absorption refrigeration systems (ARS) based on operational, health, safety, and environmental criteria. The environmental, health, and safety (EHS) profile of the solvents was previously evaluated by Viar et al. [24] using the CHEM21 solvent selection guide. In terms of their physicochemical properties and potential hazards to health and the environment, each solvent exhibited an EHS profile recommended for use in an ARS, except for terpinolene, which should be avoided in water bodies due to its impact on the marine environment.

Regarding their origin, it is worth noting that four of these solvents (Solketal, γ-Valerolactone, Rhodiasolv PolarClean, and Terpinolene) can be obtained from biomass, while Propylene Carbonate can be produced as a valorization product of captured CO_2. Table 2 collects the most relevant properties of the selected solvents for the design of ARSs, including melting, flash, boiling and autoignition temperatures, as well as vapor pressure, density, viscosity, and surface tension at 303.15 K.

Table 2
Physical properties and cost of selected organic solvents [41–52]. Vapor pressure, liquid density, viscosity and surface tension are given at 303.15 K.

Solvent	Melting point (K)	Flash point (K)	Boiling point (K)	Autoignition Temp. (K)	Vapor pressure (Pa)	Liquid density (g cm^{-3})	Viscosity (mPa s)	Surface tension (mN m^{-1})	Price (€ kg^{-1})
SKL	246.75	353.15	461.70	663.15	1.43	1.059	8.4	31.6	170
PC	220.30	405.15	514.85	728.15	6.53	1.195	2.2	40.8	60
TPN	253.15	337.15	460.15	608.15	101*	0.854	1.8*	N.A.	80
GVL	242.15	369.15	477.54	675.15	64.8	1.044	2.2	36.1	240
RPC	212.15	419.15	553.15	663.15	1.28	1.034	6.2	37.1	180

* Property at 293.15 K.

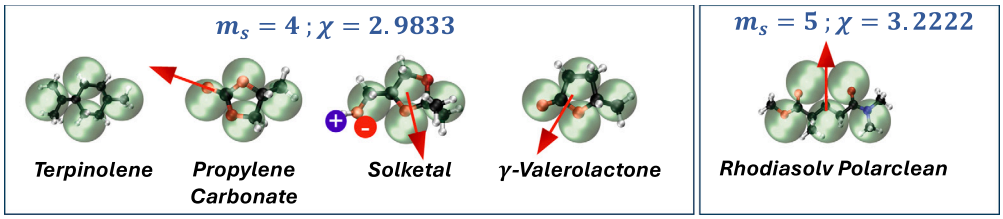

Fig. 3. Selected configurations for the bio-based solvents model. Green circles represent the ring-like structure, represented by m_s, the red arrow indicates the polar contribution, while the positive and negative circles account for SKL association nature.

As can be seen, all solvents exhibit exceptional properties for absorption refrigeration applications, including a wide liquid range (exceeding 200 K), high flash points, and particularly high boiling points, between 460 and 553 K. These characteristics are essential to ensure thermal stability over long operating times and reduced volatility (i.e., very low vapor pressures).

Moreover, the viscosity of the organic solvents was a key criterion in the screening of potential alternatives to conventional working fluids. As absorption equilibrium is often not achieved in the absorber, even for classical working pairs such as water–LiBr [53], organic solvents exhibiting very low viscosity, comparable to that of conventional working fluids, were sought to ensure practical operation. In this respect, the viscosity of the five solvents selected in this work ranges between 2 and 8 mPa s at the lowest operating solvent temperature, corresponding to the absorber temperature (303.15 K). This viscosity range is comparable to that of the water–LiBr system, which lies between 1.3 and 7.8 mPa s for mass fractions between 0.2 and 0.6 at 293.15 K [54]. In addition, it should be noted that solvent viscosity decreases (and, consequently, gas diffusivity increases), not only with temperature, but also with increasing the absorbed refrigerant concentration.

Finally, the surface tension of the selected organic solvents ranges between 30 and 40 mN/m, approximately half of that of water–LiBr solutions (86 mN/m at 308 K [53]). This lower surface tension is expected to enhance wettability and, as a result, improve mass and heat transfer rates, particularly in the absorber. Beyond their attractive physicochemical properties, these solvents are also significantly cheaper and more readily available than other alternative solvents currently under consideration, such as ILs.

4. Results

4.1. Molecular models

In this study, all bio-based solvents are assumed to follow triangular arrangements, according to their molecular conformation, with predefined values of m_s and χ, as detailed in the original work by Müller and Mejía [29]. Terpinolene (TPN), Propylene Carbonate (PC), Solketal (SKL), and γ-Valerolactone (GVL) present a ring in the core of its chemical structure, being well represented by four segments ($m_s = 4$ and $\chi = 2.9833$). In the case of Rhodiasolv PolarClean (RPC), the presence of a highly branched molecular structure, including ester and carbonyl functionalities, results in a compact molecular architecture with a reduced effective length-to-width ratio. Consequently, introducing a ring contribution provides a more appropriate representation of its molecular topology than a linear-chain model. Considering this fact and its longer length compared to the other molecules, a representation of five segments ($m_s = 5$ and $\chi = 3.2222$) is suggested. Polarity is considered for all solvents except TPN, which is treated as non-polar due to the absence of significant dipole moments. Additionally, SKL is the only one modeled with an association term. This choice is justified by the presence of a hydroxyl functional group (−OH), which enables hydrogen bonding. To accurately represent this behavior, one positive and one negative association site are assigned, noted as $[0, 1, 1]$. Fig. 3 illustrates the molecular configurations considered for the solvents under the ring-structure assumption, also indicating the presence of a polar moment and/or association.

SAFT-VR Mie parameters were initially estimated using the corresponding states method, following the methodology described by Mejía et al. [55], as a reasonable first approximation. These parameters (represented by ξ) were subsequently refined by fitting to experimental data for vapor pressure (P_{sat}) and single liquid-phase density (ρ_l) at atmospheric pressure [44,45,47,48,51], using the Objective Function (OF):

$$\mathrm{OF}(\xi) = \frac{1}{m}\sum_{i=1}^{m}\left(\frac{P_{sat,i}^{cal}}{P_{sat,i}^{exp}} - 1\right) + \frac{1}{n}\sum_{i=1}^{n}\left(\frac{\rho_{l,i}^{cal}}{\rho_{l,i}^{exp}} - 1\right) \tag{35}$$

The final list of optimized molecular parameters is depicted in Table 3, while the description of the vapor pressure and the one-phase liquid density for these fluids is graphically shown in Fig. 4. As observed, excellent agreement is found in all cases, with very minor deviations for both properties. This is particularly interesting for the vapor pressure, provided the difficulty in reproducing these low values. The highest vapor pressure relative deviation is found for RPC, still remaining below 2.3%.

Concerning the refrigerants, R32, R125, R134a, R1234ze(E) and R1234yf were modeled by considering only the polar contribution, as their molecular structures exhibit significant permanent dipole moments due to the presence of highly electronegative fluorine atoms. These dipolar interactions are effectively captured through the polar term of the equation of state, as shown in the literature with different SAFT versions integrating this term [56,57]. Although a recent contribution suggests the inclusion of quadrupolar effects in the model [57], these are considered to be effectively included in the dominant dipole

Table 3
SAFT-VR Mie molecular parameters for the bio-based solvents studied in this work and relative error on vapor pressure and liquid density.

Solvent	m_s	σ/Å	ε/k_B /K	λ_r	χ	μ_{pol}/D	n_{pol}	$\%err_{P_{sat}}$	$\%err_\rho$
TPN	4.0	3.858	256.712	10.878	2.9833	–	–	0.583	0.038
RPC	5.0	3.827	181.756	6.998	4.7188	3.50	0.509	2.225	0.049
PC	4.0	3.192	225.583	7.863	2.9833	4.95	0.182	0.974	0.261
GVL	4.0	3.291	209.764	7.965	2.9833	4.30	0.278	0.490	0.033
SKL	4.0	3.578	257.329	11.717	2.9833	2.17	0.316	≈ 0	0.038

* The model for SKL also includes an associative contribution, defined with one positive and one negative site, with a ϵ^{AB}/k_B = 1107.89 K and a r_c^{AB}/σ = 0.704.

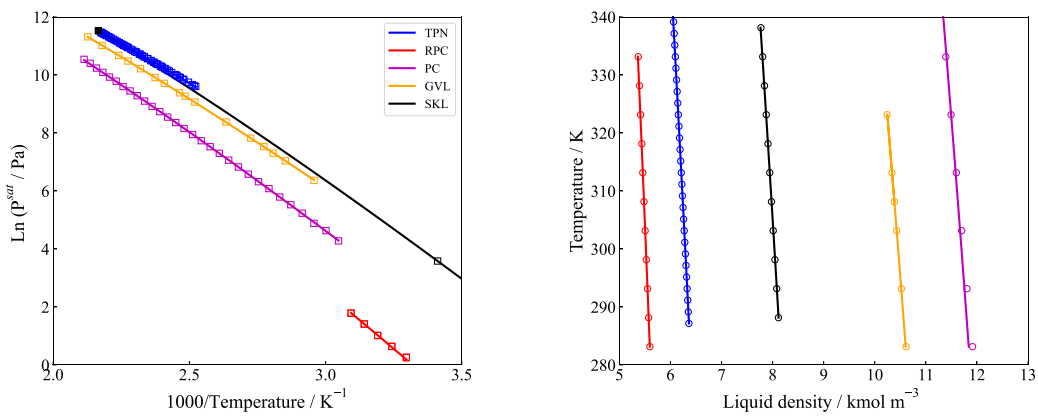

(a) (b)

Fig. 4. (a) $\ln(P^{sat})$ in the Clausius–Clapeyron representation and; (b) Liquid Density (ρ) (kmol m^{-3}) at atmospheric pressure as a function of Temperature (K) for Terpinolene (TPN, —), Rhodiasolv Polarclean (RPC, —), Propylene Carbonate (PC, —), γ-Valerolactane (GVL, —) and Solketal (SKL, —). The solid line represents the SAFT-VR Mie model, while the markers indicate the experimental data [44,45,47,48,51].

moments, and are not considered here to reduce the number of parameters included. Furthermore, CO_2 was modeled using the parameters reported in the original SAFT-VR Mie work by Dufal et al. [27], as they constitute a well-established and robust parametrization within the SAFT-VR Mie framework, having been successfully applied to systems involving different solvents and molecular environments [58–60].

The parameters for each refrigerant were fitted to experimental data for vapor pressure (P_{sat}), saturated liquid and vapor densities (ρ_l^S and ρ_v^S), and enthalpy of vaporization (ΔH_{vap}), as obtained from the CoolProp database [32].

$$\mathrm{OF}(\xi) = \frac{w_P}{n}\sum_{i=1}^{n}\left(\frac{P_{sat,i}^{cal}}{P_{sat,i}^{exp}} - 1\right) + \frac{w_{\rho_l}}{n}\sum_{i=1}^{n}\left(\frac{\rho_{l,i}^{S,cal}}{\rho_{l,i}^{S,exp}} - 1\right) + \frac{w_{\rho_v}}{n}\sum_{i=1}^{n}\left(\frac{\rho_{v,i}^{S,cal}}{\rho_{v,i}^{S,exp}} - 1\right) + \frac{w_{\Delta H_{vap}}}{n}\sum_{i=1}^{n}\left(\frac{\Delta H_{vap,i}^{cal}}{\Delta H_{vap,i}^{exp}} - 1\right) \quad (36)$$

The different weight factors are selected prioritizing the vapor pressure and saturated liquid density in the optimization, while the superscripts *cal* and *exp* represent calculated and experimental data values.

The optimized molecular parameters are depicted in Table 4, while a representation of the saturated densities, vapor pressure and enthalpy of vaporization diagrams are highlighted in Fig. 5. The inclusion of the dipolar effect into the model allows an excellent description of the whole phase envelope of the fluid, ensuring a reliable description of other properties that are predicted from the model, such as the saturated enthalpies (see Fig. 5(c)), which become crucial in evaluating the efficiency of the cycles. The relative errors in all properties remain below 2.5%, with the exception of the saturated vapor density and enthalpy of vaporization of R32, whose value increases up to around 4% due to the vicinity of the critical point.

4.2. Thermodynamic description of the working pairs

Once both, the solvents and the refrigerants, have been adequately characterized, the solubility of these F-gases in the bio-based derived solvents is addressed with the SAFT-VR Mie model. For this purpose, a binary parameter k_{ij} has been used to properly describe the interactions between these fluids using the experimental data sourced from previous work [24] at a selected temperature of 303.15 K, typical of a refrigerator absorber. In addition, new experimental data is presented for the solubility of CO_2 in these solvents. The experimental procedure details can be found in Section S.3, while the exact values of the measurements are included in Table S.3 and S.4, all in the Supplementary Material. Fig. 6 highlights the solubility of the F-gases and CO_2 in the 5 solvents at this constant temperature.

The results reveal several interesting remarks. Regardless the refrigerant studied, the highest absorption capacity is always achieved by RPC, while GVL remains in second place in most cases. On the other side, TPN appears to provide the lowest absorption in all cases, with the exception of R1234yf. The non-associative nature of TPN is clearly a handicap, reducing the capacity to interact with all gases.

If the analysis is done checking the refrigerant, it can be noticed that R1234ze(E) is the refrigerant with a higher absorption of all studied fluids, closely followed by R134a. This is an interesting fact, provided that R1234ze(E) has almost null GWP being, a priori, convenient from an environmental perspective. Interestingly, the other HFO, R1234yf, exhibits the lowest solubility among the F-gases, while R32 and R125 are in an intermediate position and very close to each other. Compared to the fluorinated refrigerants, the solubility of CO_2 is the lowest, regardless the solvent used, requiring the use of higher pressures to become competitive. Among all combinations, the highest solubility is achieved by R1234ze(E) and R134a with RPC, followed by the same systems in GVL.

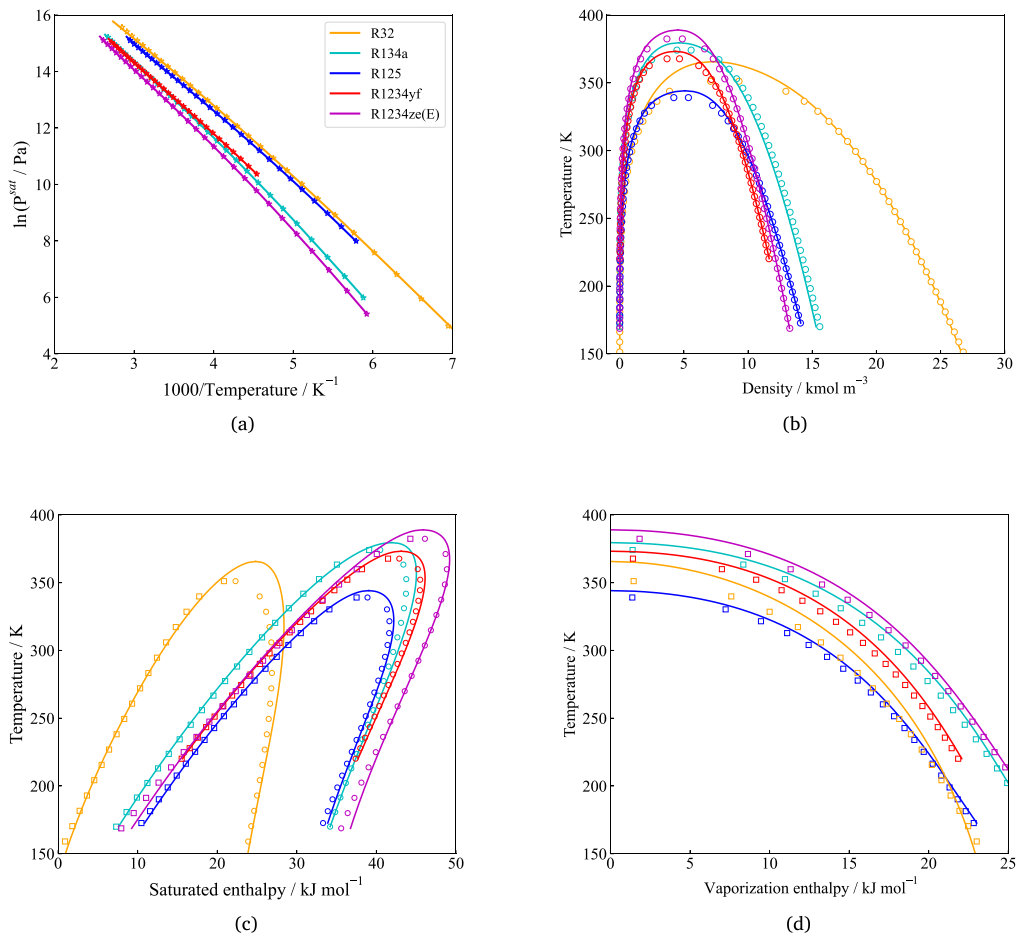

Fig. 5. Main thermophysical properties for refrigerants R134a (—), R32 (—), R125 (—), R1234yf (—), and R1234ze(E) (—). (a) $\ln(P^{sat})$ in the Clausius–Clapeyron representation; (b) saturated densities (ρ) (kmol m^{-3}); (c) saturated enthalpy (kJ mol^{-1}); and (d) vaporization enthalpy (kJ mol^{-1}). The solid line represents the SAFT-VR Mie model, while the markers indicate the experimental data.

Table 4
SAFT-VR Mie molecular parameters for the pure selected refrigerants and relative error (%) on vapor pressure, liquid and vapor saturated density and enthalpy of vaporization.

Component	m_s	σ/Å	ε/k_B /K	λ_r	μ_{pol}/D	n_{pol}	%err$_{P_{sat}}$	%err$_{\rho_L^S}$	%err$_{\rho_V^S}$	%err$_{\Delta H_{vap}}$
R134a	2.448	3.401	220.634	14.672	2.058	0.711	0.205	1.851	1.885	1.999
R32	2.422	2.835	159.060	10.479	1.978	0.782	0.599	0.139	4.016	4.344
R125	1.940	3.796	261.211	19.915	1.563	0.310	0.257	0.216	1.911	2.359
R1234yf	1.862	4.007	263.726	18.036	2.240	0.951	0.223	0.086	2.245	2.279
R1234ze(E)	1.985	3.894	287.939	19.168	1.130	0.731	0.333	0.077	1.854	1.673

From a modeling perspective, all fluids can be accurately described using a single k_{ij} binary parameter, whose value is depicted at Table 5 for each working pair, while the AAD% corresponding to the solubility curves is provided in Table S.6 of the Supplementary Material.

One important remark is the fact that most values remain close to zero, indicating that the predicted combining rule could already capture the solubility behavior of these fluids. This is a key feature for a qualitative screening of new solvents when experimental data are not available, which highlights the robustness of the thermodynamic model. In general, most corrections are negative, with the only exception of those with TPN, which are slightly positive. Negative values indicate that the predictive mixing rule (without a k_{ij} correction) underpredicts the absorption capacity of these solvents, while in the

Table 5
List of k_{ij} binary parameters for all the working pairs involved in this fluid. Values are temperature independent.

	R32	R125	R134a	R1234yf	R1234ze(E)	CO_2
TPN	0.047	0.055	0.056	0.010	0.030	0.067
RPC	−0.078	−0.133	−0.085	−0.080	−0.095	−0.052
PC	−0.053	−0.136	−0.085	−0.116	−0.111	−0.063
GVL	−0.051	−0.128	−0.074	−0.092	−0.095	−0.041
SKL	−0.036	−0.038	−0.022	−0.030	−0.026	−0.006

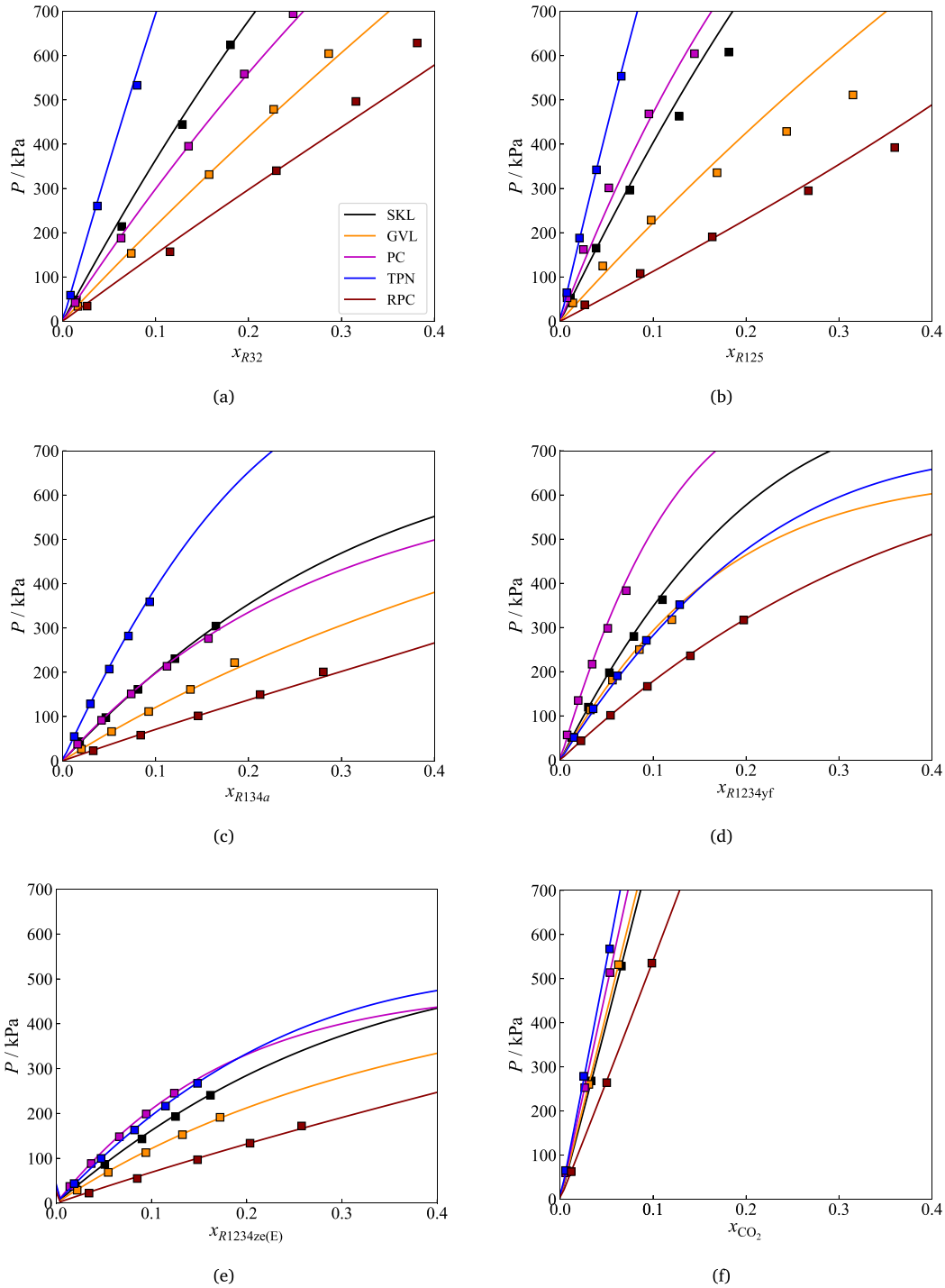

Fig. 6. Pressure-composition (P–x_1) diagrams at 303.15 K of (a) R32, (b) R125, (c) R134a, (d) R1234yf, (e) R1234ze(E) and (f) CO_2 in SKL (—), GVL (—), PC (—), TPN (—) and RPC (—). The data show the vapor pressure as a function of the mole fraction of the refrigerant (x_1). Experimental data [24] are represented by square markers, and the solid lines correspond to model or fitted predictions.

case of TPN, a slight overprediction occurs. The major corrections correspond to the PC solvent and for R125. The difficulty in modeling R125 is common, due to the effect of the 5 fluorine atoms, typically requiring larger binary parameter adjustments, as shown in literature [61].

As mentioned, the results of Fig. 6 indicate that GVL and RPC, combined with R134a and R1234ze(E), offer the highest HFC and HFO absorption capacity. However, one important aspect of an accurate thermodynamic model is their ability to describe the system at different temperatures. This is demonstrated by predicting the solubility behavior of these four combinations at five isotherms ranging from 283.15 K till 323.15 K in ranges of 10 K, as plotted in Fig. 7. The SAFT-VR Mie model is capable to precisely reproduce the solubility of all isotherms in the whole concentration range where data are available. Here, it is important to remark the impact of the ring contribution term, which accounts for the non-linear nature of the solvents. For illustration purposes, Figure S.3 in the Supporting Material compares

the performance of an alternative SAFT-VR Mie model without the ring term (using a classical linear chain term) to describe the solubility of R1234yf + GVL and R134a + RPC. The results indicate that there is a clear deterioration of the solubility description at high mole fractions of R1234yf, while the linear model fails to qualitatively describe the R134a + RPC system. This fact clearly supports the assumption that the RPC molecular structure is better represented through a ring contribution than with a linear-chain model.

Coming back to the results of Fig. 7, it is important to note that the binary parameter is kept constant and transferred to other temperatures different than 303.15 K, without a deterioration of the simulated results. This fact is particularly important when modeling the desorption process carried out at the generator of the cycle, typically done at higher temperatures. The effect of the temperature for the rest of fluids has also been described in good agreement with the experimental data and is graphically displayed in Figures S.4 and S.5 of the Supplementary Material. As an additional validation step, the solubility of CO_2 in GVL and PC was predicted along several isotherms using independent experimental data reported in the literature by other authors [58, 62]. These calculations were performed using the binary interaction parameters reported in Table 5, and the corresponding results are presented in Figure S.6 of the Supporting Material. Overall, the model predictions show very good agreement with the experimental data. In particular, the solubility of CO_2 in PC at the highest temperature considered (373.15 K) is reproduced with excellent accuracy, essentially overlapping with the experimental measurements.

Based on the validity of the model, the working capacity of each working pair has been evaluated at typical absorber and desorber (i.e. at the generator) conditions, so as to pre-screen the most promising pairs for application in an ARS. For this purpose, a standard absorber temperature of 303.15 K has been fixed to determine the solubility of the refrigerant in each solvent at the saturation pressure of the refrigerant. In a similar manner, a generator temperature of 353.15 K has been established to check the remaining gas in the solvent, at its corresponding saturated pressure, trying to reproduce the real conditions occurring in these two units of the cycle. The only exception is R32, as this compound has a critical temperature below this limit. In this particular case, a generator temperature of 351 K has been assigned. Note that the calculations at the high temperature are merely predictive, as no experimental data are available. The working capacity (WC) is then simply defined as the mass solubility difference between these two points.

$$WC = w_i(P_{abs}, T_{abs}) - w_i(P_g, T_g) \tag{37}$$

An important remark regarding the WC concerns the choice of units used in the analysis. While many authors commonly present this comparison in terms of mole fractions, since this is the unit typically provided by equation of state calculations, practical industrial refrigeration applications are more concerned with mass-based quantities. For this reason, Fig. 8 presents the results in terms of grams of refrigerant per kilogram of solvent.

Interestingly, when expressed in mass terms, R125 exhibits the highest WC, closely followed by R32 and R134a. Among the HFOs, R1234ze(E) shows the best performance, while R1234yf confirms a notably low WC. Similarly, CO_2 delivers a very modest capacity and is further disadvantaged by the requirement for higher operating pressures. Regarding the solvents, RPC and GVL still stand out as the most effective, reinforcing previous findings and clearly outperforming the other candidates.

Although the R125–RPC pair offers the highest capacity, its elevated global warming potential (GWP) raises significant environmental concerns, apart from having limited thermal properties, as will be shown later in this work. In fact, R125 is typically included to decrease the flammability of refrigerant blends. Therefore, the subsequent analysis of the absorption cycle will focus on GVL and RPC as solvents, while R125, R32, R134a, and R1234ze(E) will be selected and compared as refrigerants, with environmental considerations also incorporated into the evaluation.

4.3. Parametric analysis of cycle operating conditions

The next step of the analysis refers to the practical application of these mixtures into absorption applications. As discussed in the Introduction and the Theory sections, the current study is applied to Single-Effect and Compression-Assisted Absorption Refrigeration Systems (SE-ARS and CA-ARS, respectively). The efficiency of these systems is technically evaluated through the calculation of the Energy and Exergy Coefficient of Performance (COP, and ECOP, respectively), which are, at the same time, influenced by the selected operational conditions of the cycle. Before proceeding to a detailed screening of the 8 selected systems, a benchmark working pair is used to carry out a parametric analysis of these operating conditions. For this purpose, the mixture R134a-RPC is chosen based on its high working capacity (the second one after R125), and moderate (although still important) GWP. In particular, the impact of the generator temperature (T_g), condenser temperature (T_{cond}), evaporator temperature (T_{evap}), and compression ratio (CR) (the latter only for the CA-ARS cycle) is evaluated in terms of COP and ECOP in Fig. 9. All calculations are performed at a fixed absorber temperature of 303.15 K, T_{cond} of 303.15 K, T_{evap} of 278.15 K and CR of 1.5 (i.e. for CA-ARS), unless that corresponding variable is analyzed.

The impact of the T_g is checked in Fig. 9(a). As it can be observed, the CA-ARS clearly outperforms the energy efficiency of the SE-ARS across the examined range. This improvement is attributed to the mechanical compression step, which increases the absorber pressure and enhances the absorption capacity of the solution. However, it is important to note that the COP exhibits a clear maximum for both cycles, beyond which performance begins to decline. Increasing T_g enhances the thermal driving force for desorption, thereby reducing the circulation ratio and the sensible heat duty associated with heating the solution. At moderate T_g values, this leads to a more efficient separation in the generator and improved absorber performance, resulting in a net reduction of the total heat input per unit of cooling capacity, and hence higher COP. However, as T_g continues to rise, these benefits are offset by growing thermodynamic penalties. Higher solution temperatures in the generator and absorber amplify exergy destruction due to heat transfer across larger temperature differences, and increase the specific heat load because of larger sensible heating requirements of the solution and vapor streams. Moreover, elevated T_g intensifies the heat rejection burden in the condenser/absorber, which may become increasingly constrained near ambient conditions. The combination of these effects results in a severe increase in irreversibilities and total energy input, causing the COP to decline beyond the optimum point. Notably, the optimal generator temperature is significantly lower for the CA-ARS compared to the SE-ARS. This shift reflects the influence of mechanical compression, which reduces the circulation ratio and the generator heat duty, and allows the cycle to operate efficiently at lower T_g, as reported in the literature [10,24]. This comes at a cost of a lower ECOP in CA-ARS, because adding compression introduces high-quality exergy consumption (mechanical work), which outweighs the gains in cooling performance when measured on an exergy basis. The generator temperature maximizing the COP has been used to perform the rest of calculations of the parametric analysis.

Fig. 9(b) shows a decreasing trend in both COP and ECOP when increasing the condenser temperature. This behavior is expected, as a higher T_{cond} increases the irreversibilities associated with heat rejection, reducing the temperature lift and thus degrading the thermodynamic performance of the cycle. No performance maximum is observed within the studied range. Since the condenser must reject heat to the ambient, its temperature is inherently constrained by the external cooling medium, such as underground, surface, or evaporative cooling

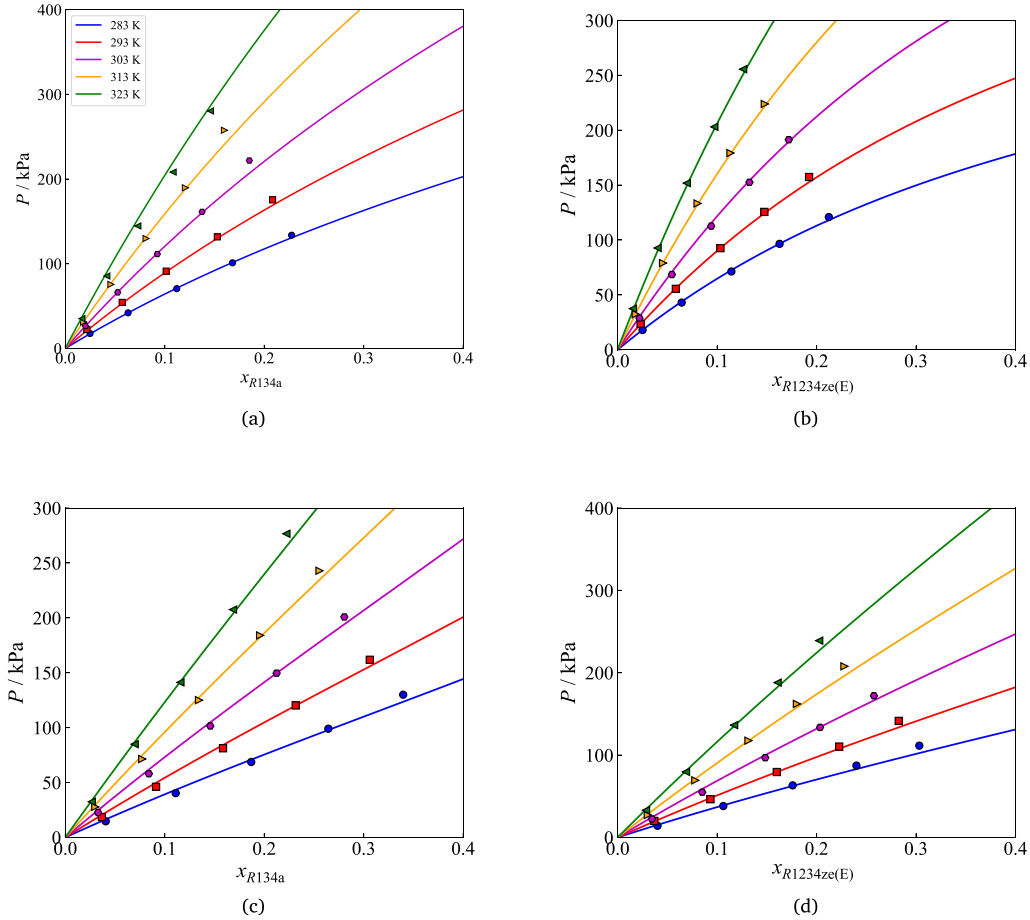

Fig. 7. Pressure-composition (P–x_1) diagrams at 283.15 K (—), 293.15 K (—), 303.15 K (—), 313.15 K (—) and 323.15 K (—) for the working pairs (a) R134a-GVL, (b) R1234ze(E)-GVL; (c) R134a-RPC; (d) R1234ze(E)-RPC. Symbols are experimental data [24] and lines correspond to the SAFT-VR Mie model.

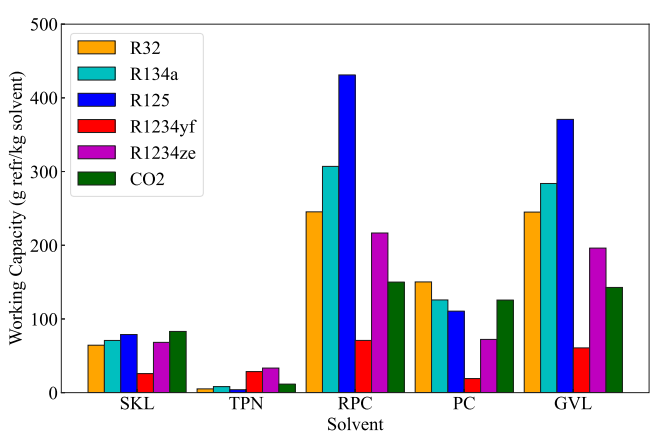

Fig. 8. Working capacity of R32 (orange), R134a (cyan), R125 (blue), R1234yf (red), R1234ze(E) (magenta), and CO_2 (green) in the five studied solvents (Solketal — SKL, Terpinolene — TPN, Rhodiasolv PolarClean — RPC, Propylene Carbonate — PC, and γ-Valerolactone — GVL). Working capacity is expressed as grams of refrigerant absorbed per kilogram of solvent.

water, or ambient air. For this reason, a reference condenser temperature of 303.15 K has been used for the rest of calculations in this work, being commonly adopted in the literature [10] to reflect standard ambient conditions and enable meaningful comparisons across systems and working pairs. Once again, the CA-ARS configuration consistently demonstrates higher COP and lower ECOP values across the range, as the mechanical assistance allows for better control over refrigerant flow and absorption/desorption dynamics, partially mitigating the negative impact of elevated condenser temperatures on system efficiency.

The influence of T_{evap} on both COP and ECOP is illustrated in Fig. 9(c). As T_{evap} increases, a marked improvement is observed in the COP performance. A higher T_{evap} rises the saturation pressure in both, the evaporator and absorber, increasing the absorption capacity of the refrigerant. As far as the concentration of the strong solution is only slightly influenced by changes in T_{evap}, the larger concentration difference between the two solutions enhances the COP. In terms of ECOP, a maximum can be found around 277 K, to later decrease with the increase of T_{evap}. The trends in SE-ARS and CA-ARS are almost identical. In any case, it is important to note that in real applications, T_{evap} is practically determined by the required cooling or refrigeration temperature, which sets the lower bound of the thermal demand (i.e. chilled water). Therefore, while the thermodynamic performance improves with increasing T_{evap}, the operational range must be carefully selected to ensure applicability in real-world scenarios. Considering these aspects, the original evaporator temperature of 278.15 K is kept to perform the rest of calculations of this contribution.

Finally, Fig. 9(d) explores the effect of the compression ratio (CR) on the performance of the CA-ARS in the range 1.2–2.0. Both COP

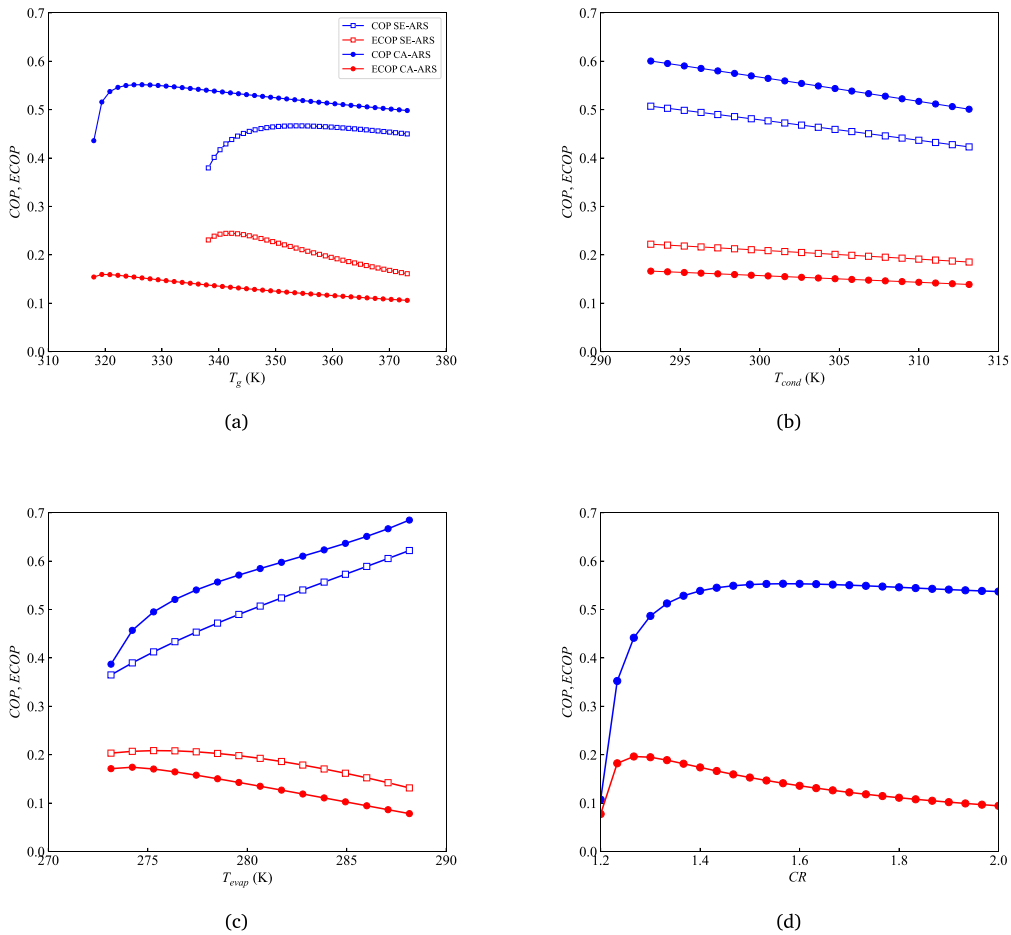

Fig. 9. Effect of the (a) generator temperature, (b) condenser temperature, (c) evaporator temperature, and (d) compression ratio on the COP: (–□–) SE, and (–•–) CA-ARSs; and ECOP: (–□–) SE, and (–•–) CA ARSs, using R134a RPC. The performance of the condenser, evaporator, and compression ratio was evaluated at the optimal generator temperatures: 353.79 K for the SE-ARS and 326.10 K for the CA-ARS.

and ECOP initially increase sharply with increasing the CR, reaching a clear maximum. Beyond this point, both indicators decline. While the reduction in COP is relatively modest and the values remain nearly constant, the ECOP exhibits a more pronounced decrease. This behavior is attributed to the growing exergy losses associated with mechanical compression, which are not proportionally compensated by improvements in system performance. Consequently, the selected CR must represent a balanced compromise between COP and ECOP. An intermediate CR value of 1.5 was therefore adopted, as it lies close to the COP optimum and is consistent with values commonly reported in the literature for CA-ARSs [10,11].

Overall, these results demonstrate that the CA-ARS offers better thermodynamic performance than the SE-ARS across all parameters in terms of energy efficiency. However, optimization must consider the trade-off between COP and ECOP, particularly in terms of the generator temperature. For this reason, this parameter will be subsequently optimized for the rest of systems, while the condenser and evaporator temperature will remain constant at $T_{\text{cond}} = 303.15$ K and $T_{\text{evap}} = 278.15$ K, respectively, with a CR of 1.5.

4.4. 3E analysis and selection of best working pair

Given the significant influence of the generator temperature (T_g) on cycle performance, this variable, along with the refrigerant circulation ratio, (f), were retained as key parameters for the analysis of the remaining working pairs selected for screening. Figs. 10(a) and 10(b) present the variation of the COP as a function T_g for the eight refrigerant–absorbent combinations, involving R32, R125, R134a, and R1234ze(E), each paired with either RPC or GVL. Fig. 10(a) corresponds to the SE cycle, while Fig. 10(b) refers to the CA configuration.

The analysis of both configurations reveals several consistent trends. First, the CA cycle yields an energy efficiency improvement of approximately 10%–20% relative to the single-effect cycle across all refrigerant–absorbent combinations. In both cases, COP exhibits a maximum as a function of T_g, with the optimal temperature significantly lower in the CA cycle due to the auxiliary mechanical compression reducing the thermal load on the generator.

In the SE cycle (Fig. 10(a)), the best performing system is R32-GVL, reaching COP values approaching 0.60, with its optimal limited by the critical temperature of the refrigerant. R134a emerges as the second-best candidate, whereas R1234ze(E) reaches a modest optimal COP of 0.465, far from the previous HFCs. R125-based systems consistently exhibit the lowest performance. This reveals that other factors, more related to the enthalpy differences, play a key role, surpassing the highest working capacity of R125 in both solvents (see Fig. 8). These trends are consistently repeated when RPC is chosen. However, the use of RPC worsens the efficiency of the cycle, producing a decline in the COP values for all refrigerants. Otherwise, the impact of the solvent is less significant when using R32, which stands out as the best working fluid, regardless of the solvent used.

Concerning the CA configuration (Fig. 10(b)), R32-GVL delivers once again the highest performance, with COP values close to 0.70.

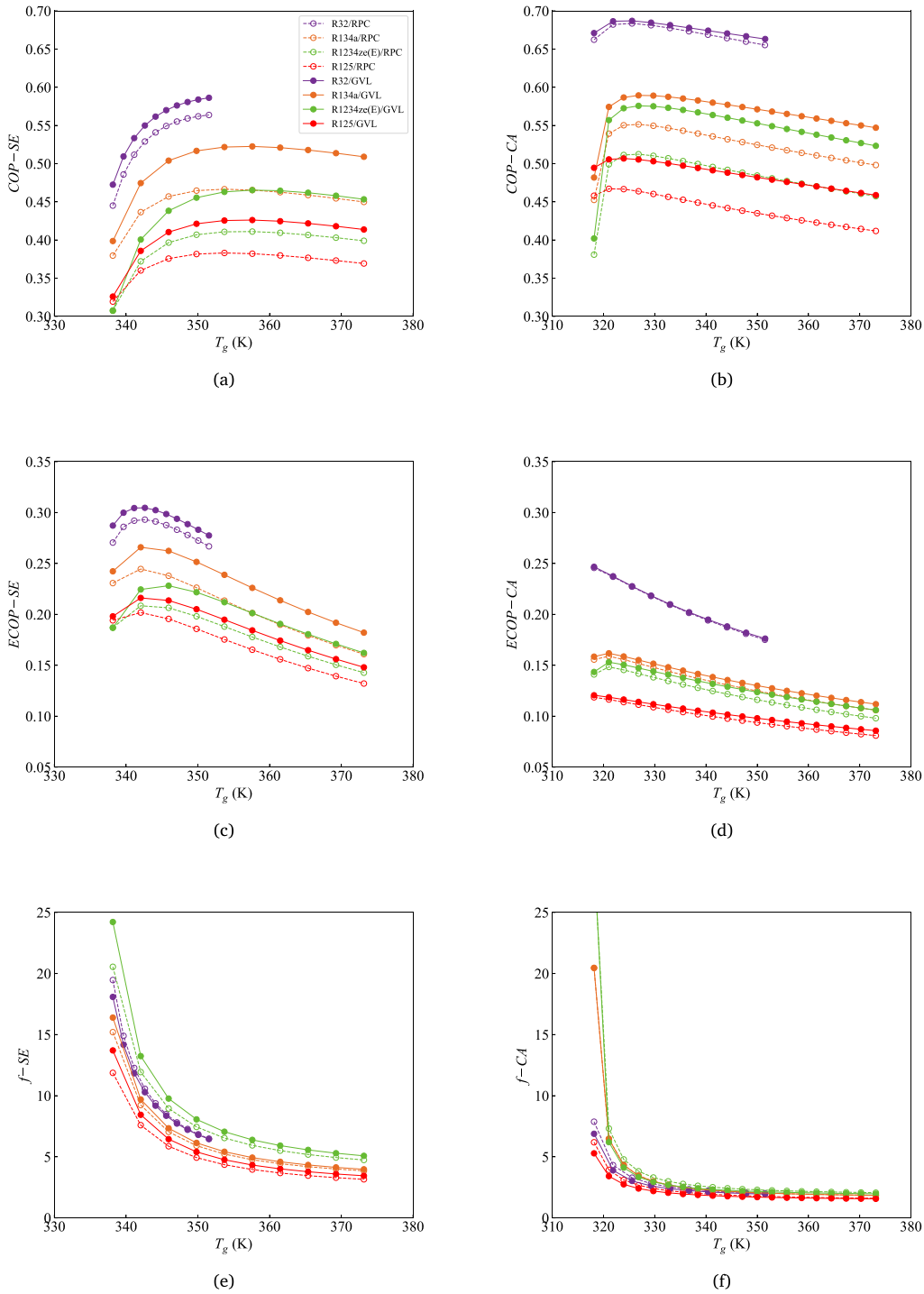

Fig. 10. Effect of the generator temperature in the (a) COP-SE, (b) COP-CA, (c) ECOP-SE, (d) ECOP-CA, (e) f-SE, and (f) f-CA using R32 (—), R134a (—), R1234ze(E) (—) and R125 (—) in GVL (—•—) and RPC (– – ∘ – –). All calculations are carried out with SAFT-VR Mie.

Notably, the performance of R1234ze(E)-GVL improves in the CA cycle, approaching COP levels to that of R134a-GVL. This indicates that compression assistance can mitigate some of the limitations observed for HFOs in the single-effect cycle, making them more competitive under favorable operating conditions.

The performance in terms of exergetic efficiency is evaluated in Figs. 10(c) and 10(d) for the SE and CA cycles, respectively. As it can be observed, higher values are obtained for the SE configuration, with R32 standing out again as the best option, followed by R134a, R1234ze(E) and R125. When moving to the CA cycle, the exergetic efficiency goes down, due to the additional irreversibilities introduced by the mechanical compressor. In addition, it is noticed that the impact of the solvent is not remarkable in the CA cases.

Finally, the amount of refrigerant needed is plotted, in terms of circulation ratio, in Figs. 10(e) and 10(f) as a function of T_g for the SE and CA cycles, respectively. As expected, f decreases with increasing

T_g, reflecting enhanced desorption efficiency at higher temperatures and, consequently, a reduced need for refrigerant recirculation per unit of cooling. However, while this reduction is more gradual in SE configuration, it occurs very sharply in the CA cycle. Indeed, the amount of refrigerant remained almost constant after 330 K, where further increases in T_g yield marginal gains. This behavior is related to the optimal COP reached by all systems, whose value is attained at low temperatures in the CA cycles. In terms of refrigerant, R125 has the lowest (and best) circulation ratio, which coincides with its higher WC, as previously commented. In this regard, R1234ze(E) is the compound that requires a higher amount of fluid circulating. In terms of the solvent, the use of RPC slightly reduces the circulation ratio, as expected from the results obtained when analyzing the WC of all refrigerant pairs (see Fig. 8). However, as seen before, this is not reflected in a higher energy efficiency of the system.

The previous analysis only concerns technical factors. However, it is important to account for the environmental constraints to decide about the best working pair. While GWP offers a first and practical vision of the environmental impact in terms of CO_2 emissions, it is also important to consider other indirect effects, typically emerging from associated emissions to leakage, electricity production, etc. As explained in Section 2.4, TEWI has been used as a metric to evaluate the environmental performance of these systems, and to estimate the total contribution of a refrigeration system to global warming over its entire lifetime. For this purpose, calculations have been estimated based on an ARS with a cooling capacity of 10 kW, representative of a small refrigeration application (i.e. production of chilled water at ≈5 °C to cool a restaurant dining room of around 100 m^2) that will be working 3000 h/year. The refrigerant charge, m, is fixed at 2.0 kg, in agreement with specific charge-to-capacity ratios reported in the literature for chillers using fluorinated refrigerants (≈0.2 kg kW^{-1}) [63]. Moreover, it is assumed that the energy required in the generator is residual waste heat coming from gas-fired cooking appliances (i.e. gas ovens), which is considered to have zero marginal CO_2 emissions. This assumption is in accordance with standard TEWI practice for heat-driven systems, where energy inputs that do not change the system marginal emissions are excluded [64]. While this choice will reduce the magnitude of indirect emissions, representing the best case scenario, it does not alter the qualitative comparison among working pairs. The rest of required parameters are described in Section 2.4.

The results for the different refrigerants are plotted in Fig. 11 for the CA-ARS case. Here, it is important to note that the effect of the solvent is not explicitly considered, as the solvent does not have GWP and does not go through the compressor of the system in the CA-cycle process. Consequently, it is assumed that the emissions are fully-dependent on the refrigerant. Interestingly, it can be seen that indirect emissions represent the most important part of the environmental penalty, representing more than 95% of the total emissions. This statement is in agreement with observations in VCRCs [38]. More importantly, this calculation highlights the prevalence of using a refrigerant with a good cooling capacity, such as R32, which provides the lowest total emissions, given its moderate GWP and good technical efficiency, which reduces the compressor work. Although R1234ze(E) has practically no direct emissions (orange bar value is 0.002 $tCO_2eq\ y^{-1}$), its indirect emissions coming from a lower efficiency are of a similar order than those of R134a and close to double than that of R32. Finally, the use of R125 appears to be the worst option, being the only case where direct emissions reach 10% of the total (caused due to its high GWP), and higher indirect emissions, as a consequence of a lower efficiency, as shown in Figs. 10(a) and 10(b). It is important to note that, although TEWI provides a useful first-level indicator to compare the environmental performance of alternative working pairs under consistent operating assumptions, it does not account for upstream and downstream impacts associated with solvent production, transportation, and end-of-life management. A complete life-cycle assessment (LCA) would be required to capture these contributions in all. However, such an analysis is beyond the scope of this preliminary screening study and is identified as an important avenue for future work once a specific system configuration is selected.

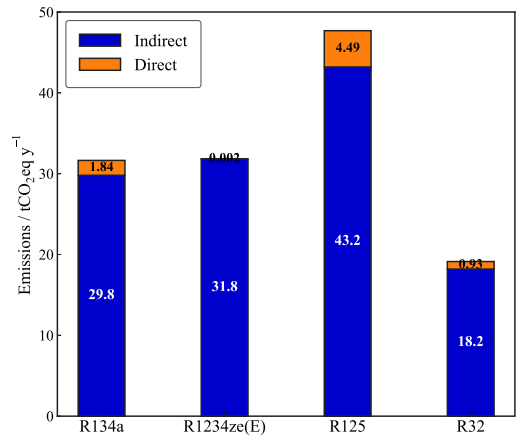

Fig. 11. TEWI emissions using different refrigerants. The orange section represents direct emissions, while the blue section accounts for indirect emissions.

Finally, five KPIs were selected to provide an overall assessment of all options, covering energy, exergy, and environmental indicators: COP, ECOP, generator pressure (P_g), circulation ratio (f) and TEWI. The analysis for each working pair was performed at the generator temperature corresponding to its maximum COP, with the ECOP, P_g, f and TEWI values evaluated at that temperature. Consequently, the working pairs are compared under thermodynamic conditions to which they are best adapted. These 5 items are summarized in Table 6 and were subsequently normalized between 0 and 1 for graphical representation, being zero the worst value and one the best among the studied options. Consequently, a value of 1 corresponds to the maximum COP and ECOP, while it represents the minimum P_g, f, and TEWI. The results were plotted in radar graphics for a visual inspection in Fig. 12. In particular, Figs. 12(a) and 12(b) refer to SE-ARS when using GVL and RPC, respectively, while Figs. 12(c) and 12(d) are devoted to the CA-ARSs. As a general trend, the COP values are systematically higher for CA-ARS, while the ECOP and the environmental performance in SE-ARS is consistently better, because of the lack of irreversibilities and indirect emissions related to compressor work.

In terms of efficiency, the radar plots clearly display that R32 (red) stands out with the highest COP and ECOP values, and notable TEWI, reflecting its potential as the best refrigerant, at the cost of the highest P_g. R134a (blue) consistently displays a very balanced performance across all indicators, becoming the second best option in practically all KPIs. As a result, it shows the biggest area for SE-ARSs. Interestingly, R1234ze(E) (orange) offers a different performance when the system configuration is changed. For the SE-ARS, it has the best sustainability index and the lowest P_g, but remains with a very modest efficiency, also requiring a high circulation ratio. When checking its performance for CA-ARS, R1234ze(E) provides a more competitive COP and f, being outperformed by R32 in terms of TEWI because of a higher amount of indirect emissions. In contrast, R125 (green) shows the worst performance in all factors, with the only exception of a competitive circulation ratio, as it was expected from the previous WC analysis. Overall, the picture does not offer remarkable differences between solvents, with a slight superior performance of GVL. The shaded areas suggest that R134a-GVL is the best choice for SE-ARS, while R32-GVL is more adequate in CA-ARS.

While the radar plots of Fig. 12 allow to identify the most promising working pairs, they do provide equal weight to all KPIs. This may result in a wrong interpretation of the best working pair for each cycle.

Table 6
Key performance indicators and TOPSIS analysis for Single-Effect and Compression-Assisted ARSs.

Single-Effect ARS										
Mixture	T_g/K	COP	ECOP	f	P_g/kPa	TEWI	S^+	S^-	Score	Rank
R134a-GVL	356.7	0.523	0.229	5.02	770	1.22	0.090	0.138	0.604	4
R1234ze(E)-GVL	358.3	0.465	0.199	6.28	577	0.002	0.114	0.146	0.561	8
R125-GVL	356.5	0.426	0.187	4.42	1565	3.00	0.094	0.127	0.575	6
R32-GVL	351.6	0.586	0.278	6.44	1920	0.62	0.093	0.146	0.612	1
R134a-RPC	353.8	0.467	0.213	5.20	770	1.22	0.088	0.137	0.610	2
R1234ze(E)-RPC	356.1	0.411	0.182	6.13	577	0.002	0.109	0.144	0.569	7
R125-RPC	353.7	0.383	0.175	4.34	1565	3.00	0.090	0.127	0.583	5
R32-RPC	351.6	0.564	0.267	6.48	1920	0.62	0.092	0.144	0.610	3
Compression-Assisted ARS										
Mixture	T_g/K	COP	ECOP	f	P_g/kPa	TEWI	S^+	S^-	Score	Rank
R134a-GVL	327.7	0.589	0.154	2.94	770	31.6	0.064	0.067	0.510	3
R1234ze(E)-GVL	327.5	0.576	0.147	3.22	1920	31.8	0.101	0.089	0.470	5
R125-GVL	323.4	0.507	0.117	2.84	1565	47.7	0.112	0.063	0.362	7
R32-GVL	323.9	0.687	0.232	3.15	577	19.2	0.045	0.101	0.695	1
R134a-RPC	326.1	0.552	0.153	3.62	770	31.6	0.065	0.065	0.502	4
R1234ze(E)-RPC	325.9	0.513	0.143	4.06	1920	31.8	0.102	0.088	0.464	6
R125-RPC	322.1	0.467	0.116	3.57	1565	47.7	0.112	0.062	0.355	8
R32-RPC	324.4	0.684	0.230	3.51	577	19.2	0.048	0.099	0.674	2

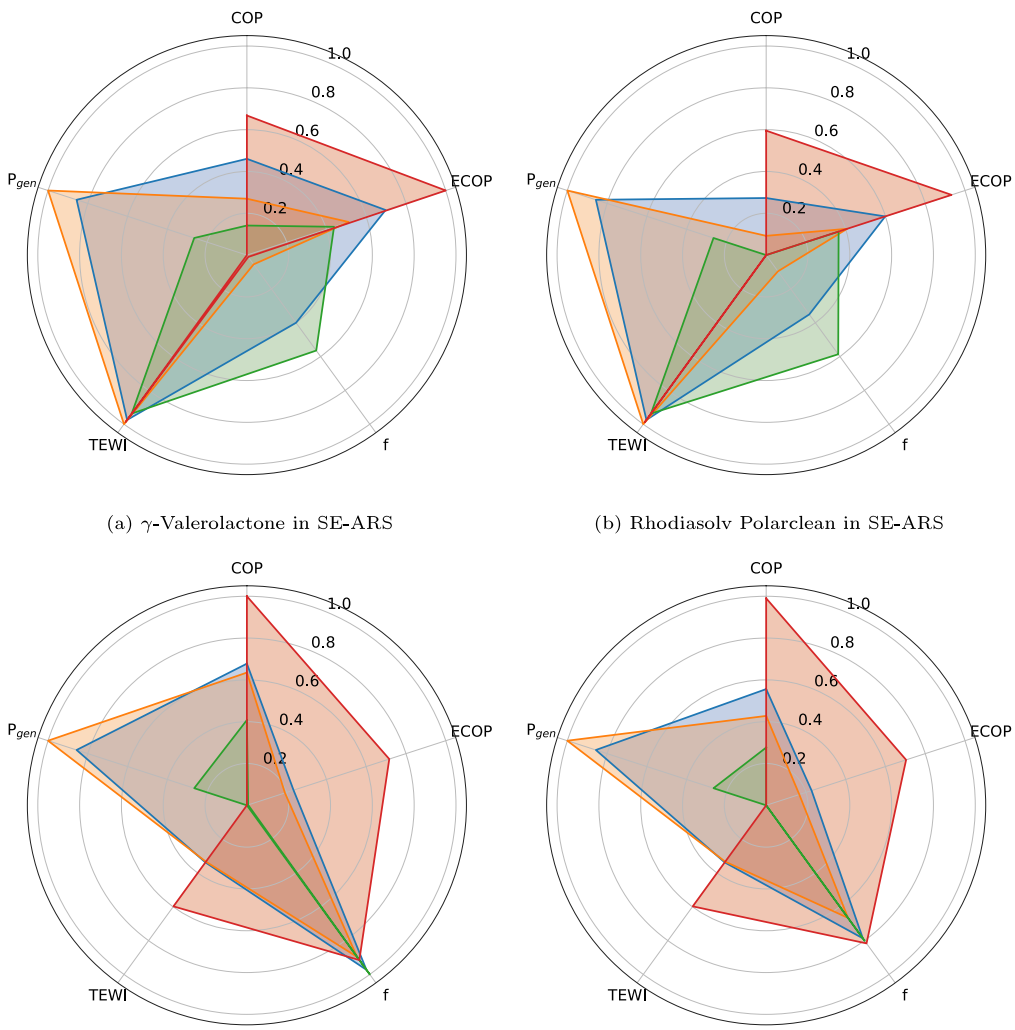

(a) γ-Valerolactone in SE-ARS (b) Rhodiasolv Polarclean in SE-ARS

(c) γ-Valerolactone in CA-ARS (d) Rhodiasolv Polarclean in CA-ARS

Fig. 12. Radar charts representing the normalized performance indicators of absorption refrigeration systems for different refrigerant–solvent combinations using (a) γ-Valerolactone (GVL) in SE-ARS, (b) Rhodiasolv Polarclean (RPC) in SE-ARS, (c) γ-Valerolactone (GVL) in CA-ARS, and (d) Rhodiasolv Polarclean (RPC) in CA–ARS as absorbents. Shaded area colors correspond to the refrigerants: R134a (●), R1234ze(E) (●), R125 (●), and R32 (●). Each axis corresponds to a key performance indicator: Coefficient of Performance (COP), Exergetic COP (ECOP), generator pressure (P_{gen}), Total Warming Environmental Impact (TEWI), and circulation ratio (f). Values are normalized between 0 and 1. Higher values reflect better performance.

In order to finally decide about the best pair, the TOPSIS methodology [39] has been applied. As explained in Section 2.5, a hybrid method based on a qualitative assessment of the relative importance of each indicator was combined with the statistical EWM to define the weights for each KPI using Eq. (30). The expert-based weighting scheme was defined to reflect the relative importance of the different performance indicators in the assessment of ARSs. The highest weight was assigned to the coefficient of performance (COP, 0.35 in both configurations), as it directly represents the thermodynamic efficiency of the cycle and strongly influences the required heat input, system size, and overall feasibility. Closely related to this, the exergy coefficient of performance (ECOP) was given a high weight (0.25 for SE-ARS and 0.20 for CA-ARS), since it accounts for auxiliary energy requirements and therefore provides a more realistic measure of system performance under practical operating conditions. The circulation factor was also assigned a significant weight (0.25 for the SE and 0.20 for the CA configurations), as it directly affects solution flow rates, heat exchanger sizing, and pumping requirements, all of which have a strong impact on system complexity and cost. In contrast, the generator pressure was given a lower weight (0.05 in both cases), since its influence is mainly associated with mechanical design constraints rather than overall performance or environmental impact. Finally, the relative importance of the TEWI indicator was adjusted to reflect the intrinsic differences between the two configurations, with a lower weight for the single-stage system (0.10) due to the lack of indirect emissions and low leakage rate, and a higher weight for the compression-assisted system (0.20), owing to the presence of mechanical compression, auxiliary electricity consumption, and a higher potential for refrigerant leakage. The combination of these qualitative weights with the statistical values from the EWM provides the final weights, which are included in Table S2 of the Supporting Material.

The results of the TOPSIS analysis are ranked in Table 6 and confirm some previous evidences, while providing some additional information. For the CA-ARS, the analysis confirms that R32-GVL stands out as the best working pair, closely followed by R32-RPC. Clearly, the impact of the refrigerant is more important than the solvent among the two studied options. The choice of R32 provides the best energetic and exergetic performance, having a moderate GWP but modest indirect emissions, becoming the most balanced option. Interestingly, when moving to the SE cycle, the situation changes and R134a competes with R32 as the best refrigerant. Indeed, the highest performance is still achieved using R32, but the differences respect to other options become marginal. This fact is a consequence of a lower difference in terms of technical efficiency (compared to the CA-ARS), as well as the removal of the indirect emissions effect of the compressor. Otherwise, this is a proof that the working-pair choice will be influenced by the type of configuration selected. Finally, it is worth noting that moderate variations in the weighting parametrization do not alter the qualitative ranking or the main trends identified by the TOPSIS analysis, confirming the robustness of the conclusions drawn from this multi-criteria assessment.

5. Concluding remarks

This work presented a unified molecular-to-process framework, based on the SAFT-VR Mie thermodynamic model, to assess the performance of new working pairs combining biomass-derived solvents with five fluorinated refrigerants and CO_2 for applications in sustainable absorption refrigeration systems.

The extended SAFT-VR Mie equation of state was used to describe Terpinolene (TPN), Propylene Carbonate (PC), Solketal (SKL), Rhodiasolv PolarClean (RPC), and γ-Valerolactone (GVL), developing molecular models that explicitly account for association, polarity, cyclic and branched molecular structures. As a result, vapor pressures and liquid densities of these compounds were reproduced with average deviations below 2.7% in all cases. In a similar manner, the saturated liquid density, vapor pressure, and enthalpy of vaporization of R32, R134a, R125, R1234yf, and R1234ze(E) were reproduced with high accuracy, with relative errors ranging from 0.2% to 4.4%.

The solubility of these refrigerants in the selected solvents was evaluated at 303.15 K, showing excellent agreement with experimental data using a single, temperature-independent binary interaction parameter. In addition, new experimental measurements for CO_2 solubility were carried out, enabling the inclusion of this compound within the same modeling framework. Among the refrigerants, R1234ze(E) and R134a exhibited the highest solubility, while GVL and RPC were identified as the solvents with the most favorable absorption properties. The binary interaction parameter was successfully transferred to other temperatures, demonstrating strong predictive capabilities over a wide range of conditions (283–323 K), with average deviations of approximately 5%.

Building on this thermodynamic foundation, the working capacity (WC) of 30 different working pairs was evaluated under standardized absorption–desorption conditions. RPC and GVL were confirmed as the most promising absorbents, while R125 showed the highest WC (approximately 450 g kg^{-1} in RPC), followed by R134a, R32, and R1234ze(E). These two solvents and four refrigerants were therefore selected for subsequent cycle-level evaluation in both single-effect (SE) and compression-assisted (CA) absorption refrigeration systems (ARSs). A prior parametric analysis using the benchmark working pair R134a-RPC demonstrated that CA-ARS configurations significantly enhance system performance and confirmed that the generator temperature must be optimized to maximize cycle efficiency, whereas condenser and evaporator temperatures follow approximately linear trends and are mainly constrained by external operating conditions.

Subsequently, a comprehensive 3E (energy, exergy, and environmental) analysis was conducted for the eight selected working pairs using five key performance indicators: COP, ECOP, circulation ratio, generator pressure, and TEWI. In all cases, the CA cycle yields an energy efficiency improvement of approximately 10%–20% relative to the SE cycle across all refrigerant–absorbent combinations. The results show that R32-GVL achieves the highest energetic and exergetic efficiencies in both SE (COP ≈ 0.59, ECOP ≈ 0.28) and CA (COP ≈ 0.69, ECOP ≈ 0.23) configurations, while the high working capacity of R125 is penalized by its lower enthalpy of vaporization. Overall, the choice of the refrigerant was found to be more determinant than the choice of the solvent. The inclusion of the TEWI analysis, while providing only a partial environmental picture, reveals that indirect emissions account for more than 90%–95% of total emissions. Consequently, although R1234ze(E) exhibits a very low GWP, its lower cycle efficiency in CA-ARS leads to higher compression work and, therefore, higher indirect emissions compared to R32.

Finally, the application of the TOPSIS multi-criteria decision-making method, using hybrid weights that combine expert judgment with the entropy weight method (EWM), confirms the superior overall performance of R32-GVL, particularly in CA-ARS configurations, while R134a-GVL also emerges as a competitive option in SE-ARS systems. Conversely, the potential environmental benefits of R1234ze(E) are outweighed by its technical limitations under the conditions analyzed. These findings further support ongoing research efforts aimed at selectively recovering R32 from waste refrigerant mixtures collected from end-of-life equipment [65,66], thereby promoting a more sustainable and circular model for the refrigeration sector.

Overall, this integrative approach, combining molecular modeling, advanced thermodynamic equations of state, cycle-level energy and exergy analysis, and environmental assessment, provides a robust and transferable pathway for the rational design and selection of next-generation refrigerant–absorbent pairs for eco-efficient thermal systems.

CRediT authorship contribution statement

Isaías Huenuvil-Pacheco: Writing – original draft, Software, Investigation. **Miguel Viar:** Investigation, Conceptualization. **Gabriel Zarca:** Methodology, Formal analysis. **Ane Urtiaga:** Writing – review & editing, Project administration. **Andrés Mejía:** Writing – review & editing, Validation, Resources. **Fèlix Llovell:** Writing – review & editing, Supervision, Funding acquisition.

Declaration of competing interest

The authors declare that they have no known competing financial interests or personal relationships that could have appeared to influence the work reported in this paper.

Acknowledgments

This research is funded by MICIU/AEI/10.13039/501100011033 through projects TED2021-130959B-I00 and TED2021-129844B-I00 (European Union NextGenerationEU/PRTR), and projects PID2022-138028OB-I00 and PID2023-149713OB-I00 (ERDF/EU). Additional support from the Chilean National Agency for Research and Development (Agencia Nacional de Investigación y Desarrollo de Chile, ANID) under FONDECYT Project 1230654, from the Chair on Energy Transition URV-Fundación Repsol, and from AGAUR as Consolidated Research Group for AGACAPE (SGR 2021-00738), is gratefully acknowledged. Finally, I. H.-P. thanks the financial support from ANID – Subdirección de Capital Humano, Beca Doctorado Nacional/2022-21222234, and M. V. thanks the FPU grant (FPU22/04137) awarded by the Spanish Ministry of Education and Professional Training.

Appendix A. Supplementary data

Supplementary material related to this article can be found online at https://doi.org/10.1016/j.energy.2026.140108.

Data availability

Data will be made available on request.

References

[1] Holechek JL, Geli HME, Sawalhah MN, Valdez R. A global assessment: Can renewable energy replace fossil fuels by 2050? Sustainability 2022;14(8). http://dx.doi.org/10.3390/su14084792.
[2] Zhang X, Xue R, Zhou R, Xia F, Yu Y, Zhang X. Research on the optimal absorption refrigeration configurations of screened low-GWP organic working fluids via pinch technology. Energy 2025;320:135429. http://dx.doi.org/10.1016/j.energy.2025.135429.
[3] Srikhirin P, Aphornratana S, Chungpaibulpatana S. A review of absorption refrigeration technologies. Renew Sustain Energy Rev 2001;5(4):343–72. http://dx.doi.org/10.1016/S1364-0321(01)00003-X.
[4] Shahad H, Hadi N. In: Overview of Working Pair used in Absorption Refrigeration Technologies, vol. 6, 2018.
[5] Ji L, Shukla SK, Zuo Z, Lu X, Ji X, Wang C. An overview of the progress of new working pairs in absorption heat pumps. Energy Rep 2023;9:703–29. http://dx.doi.org/10.1016/j.egyr.2022.11.143.
[6] Papadopoulos AI, Kyriakides A-S, Seferlis P, Hassan I. Absorption refrigeration processes with organic working fluid mixtures-a review. Renew Sustain Energy Rev 2019;109:239–70. http://dx.doi.org/10.1016/j.rser.2019.04.016.
[7] Wang L, He L, He Y. Review on absorption refrigeration technology and its potential in energy-saving and carbon emission reduction in natural gas and hydrogen liquefaction. Energies 2024;17(14). http://dx.doi.org/10.3390/en17143427.
[8] Kong D, Zhou S, Fan M, Sun W, Wang D, He G. Prediction and performance evaluation of low-GWP refrigerant/organic solvent working pairs in absorption refrigeration system. Energy 2025;328:136440. http://dx.doi.org/10.1016/j.energy.2025.136440.
[9] Kim YJ, Kim S, Joshi YK, Fedorov AG, Kohl PA. Thermodynamic analysis of an absorption refrigeration system with ionic-liquid/refrigerant mixture as a working fluid. Energy 2012;44(1):1005–16. http://dx.doi.org/10.1016/j.energy.2012.04.048.
[10] Wu W, Zhang H, You T, Li X. Thermodynamic investigation and comparison of absorption cycles using hydrofluoroolefins and ionic liquid. Ind Eng Chem Res 2017;56(35):9906–16. http://dx.doi.org/10.1021/acs.iecr.7b02343.
[11] Wu W, You T, Zhang H, Li X. Comparisons of different ionic liquids combined with trans-1, 3, 3, 3-tetrafluoropropene (r1234ze (e)) as absorption working fluids. Int J Refrig 2018;88:45–57. http://dx.doi.org/10.1016/j.ijrefrig.2017.12.011.
[12] Wu W, Leung M, Ding Z, Huang H, Bai Y, Deng L. Comparative analysis of conventional and low-GWP refrigerants with ionic liquid used for compression-assisted absorption cooling cycles. Appl Therm Eng 2020;172:115145. http://dx.doi.org/10.1016/j.applthermaleng.2020.115145.
[13] Asensio Delgado JM, Asensio Delgado S, Zarca Lago G, Urtiaga Mendia AM, et al. Analysis of hybrid compression absorption refrigeration using low-GWP HFC or HFO/ionic liquid working pairs. Int J Refrig 2022;134:232–41. http://dx.doi.org/10.1016/j.ijrefrig.2021.11.013.
[14] Huang C, Shao S, Wang N, Guo Y, Wu W. Performance analysis of compression-assisted absorption refrigeration-heating system for waste heat recovery of liquid-cooling data center. Energy 2024;305:132325. http://dx.doi.org/10.1016/j.energy.2024.132325.
[15] Zhang X, Cai L, Chen T, Liu J, Zhang X. Thermodynamic screening and analysis of ionic liquids as absorbents paired with low-GWP refrigerants in absorption refrigeration systems. Energy 2023;282:128414. http://dx.doi.org/10.1016/j.energy.2023.128414.
[16] Chu J, He M, Kontogeorgis GM, Liu X, Liang X. Screening HFC/HFO and ionic liquid for absorption refrigeration at the atomic scale by the prediction model of machine learning. Green Chem Eng 2025;6(3):357–64. http://dx.doi.org/10.1016/j.gce.2024.07.004.
[17] Li K, Wu W, Liang K, Zhang H. Simulation on key influencing factors of CO2-ionic liquid mixture compression-absorption refrigeration cycle based on aspen plus. Int Commun Heat Mass Transfer 2025;161:108506. http://dx.doi.org/10.1016/j.icheatmasstransfer.2024.108506.
[18] de Jesus SS, Maciel Filho R. Are ionic liquids eco-friendly? Renew Sustain Energy Rev 2022;157:112039. http://dx.doi.org/10.1016/j.rser.2021.112039.
[19] Martins MAR, Pinho SP, Coutinho JAP. Insights into the nature of eutectic and deep eutectic mixtures. J Solut Chem 2019;48(7):962–82. http://dx.doi.org/10.1007/s10953-018-0793-1.
[20] Abedin R, Heidarian S, Flake JC, Hung FR. Computational evaluation of mixtures of hydrofluorocarbons and deep eutectic solvents for absorption refrigeration systems. Langmuir 2017;33(42):11611–25. http://dx.doi.org/10.1021/acs.langmuir.7b02003.
[21] Abedin R, Shen Y, Flake JC, Hung FR. Deep eutectic solvents mixed with fluorinated refrigerants for absorption refrigeration: A molecular simulation study. J Phys Chem B 2020;124(22):4536–50. http://dx.doi.org/10.1021/acs.jpcb.0c01860.
[22] Haghbakhsh R, Peyrovedin H, Raeissi S, Duarte ARC, Shariati A. Investigating the performance of novel green solvents in absorption refrigeration cycles: Energy and exergy analyses. Int J Refrig 2020;113:174–86. http://dx.doi.org/10.1016/j.ijrefrig.2020.01.013.
[23] Imas C, González J, Llovell F, Garrido JM, Quinteros-Lama H. Deep eutectic solvents and traditional refrigerants in absorption refrigeration cycles using molecular approaches. Energy 2024;308:133048. http://dx.doi.org/10.1016/j.energy.2024.133048.
[24] Viar M, Pardo F, Zarca G, Urtiaga A. Biomass-derived solvents and low-GWP refrigerants as working fluids for sustainable absorption refrigeration. ACS Sustain Chem Eng 2025;13(21):7728–39. http://dx.doi.org/10.1021/acssuschemeng.5c00258.
[25] Lafitte T, Apostolakou A, Avendaño C, Galindo A, Adjiman CS, Müller EA, Jackson G. Accurate statistical associating fluid theory for chain molecules formed from mie segments. J Chem Phys 2013;139(15). http://dx.doi.org/10.1063/1.4819786.
[26] Chapman WG, Gubbins KE, Jackson G, Radosz M. New reference equation of state for associating liquids. Ind Eng Chem Res 1990;29(8):1709–21. http://dx.doi.org/10.1021/ie00104a021.
[27] Dufal S, Lafitte T, Haslam AJ, Galindo A, Clark GN, Vega C, and GJ. The a in SAFT: developing the contribution of association to the Helmholtz free energy within a wertheim TPT1 treatment of generic mie fluids. Mol Phys 2015;113(9–10):948–84. http://dx.doi.org/10.1080/00268976.2015.1029027.
[28] Gross J, Vrabec J. An equation-of-state contribution for polar components: dipolar molecules. AIChE J 2006;52(3):1194–204. http://dx.doi.org/10.1002/aic.10683.
[29] Müller EA, Mejía A. Extension of the SAFT-VR mie EoS to model homonuclear rings and its parametrization based on the principle of corresponding states. Langmuir 2017;33(42):11518–29. http://dx.doi.org/10.1021/acs.langmuir.7b00976.
[30] Huang SH, Radosz M. Equation of state for small, large, polydisperse, and associating molecules. Ind Eng Chem Res 1990;29:2284–94. http://dx.doi.org/10.1021/ie00107a014.
[31] Tan SP, Adidharma H, Radosz M. Generalized procedure for estimating the fractions of nonbonded associating molecules and their derivatives in thermodynamic perturbation theory. Ind Eng Chem Res 2004;43:203–8. http://dx.doi.org/10.1021/ie034041q.

[32] Bell IH, Wronski J, Quoilin S, Lemort V. Pure and pseudo-pure fluid thermophysical property evaluation and the open-source thermophysical property library CoolProp. Ind Eng Chem Res 2014;53(6):2498–508. http://dx.doi.org/10.1021/ie4033999.
[33] Mejía A, Müller EA, Chaparro Maldonado G. SGTPy: A python code for calculating the interfacial properties of fluids based on the square gradient theory using the SAFT-VR mie equation of state. J Chem Inf Model 2021;61:1244–50. http://dx.doi.org/10.1021/acs.jcim.0c01324.
[34] Herold KE, Radermacher R, Klein SA. Absorption chillers and heat pumps. CRC Press; 2016.
[35] The Australian Institute of Refrigeration, Air Conditioning and Heating (AIRAH). Methods of calculating total equivalent warming impact (TEWI) 2012: Best practice guidelines. Melbourne, Australia: AIRAH; 2012, Prepared by Expert Group with contributions from Jonathan Fryer, Kevin Lee, and Tony Queenin. URL https://www.airah.org.au.
[36] IPCC. 2019 refinement to the 2006 IPCC guidelines for national greenhouse gas inventories. In: 2019 refinement to the 2006 IPCC guidelines for national greenhouse gas inventories, vol. 3, Geneva, Switzerland: Intergovernmental Panel on Climate Change; 2019, Chapter 7 : Emissions of Fluorinated Substitutes for Ozone-Depleting Substances.
[37] Makhnatch P, Khodabandeh R. The role of environmental metrics (GWP, TEWI, LCCP) in the selection of low GWP refrigerant. Energy Procedia 2014;61:2460–3. http://dx.doi.org/10.1016/j.egypro.2014.12.023, International Conference on Applied Energy, ICAE2014.
[38] Albà C, Alkhatib I, Llovell F, Vega L. Hunting sustainable refrigerants fulfilling technical, environmental, safety and economic requirements. Renew Sustain Energy Rev 2023;188:113806. http://dx.doi.org/10.1016/j.rser.2023.113806.
[39] Hwang C-L, Yoon K. Multiple attribute decision making: Methods and applications. Berlin Heidelberg: Springer-Verlag; 1981.
[40] Elena Arce M, Saavedra Á, Míguez JL, Granada E. The use of grey-based methods in multi-criteria decision analysis for the evaluation of sustainable energy systems: A review. Renew Sustain Energy Rev 2015;47:924–32. http://dx.doi.org/10.1016/j.rser.2015.03.010.
[41] Ding MS. Liquid- solid phase equilibria and thermodynamic modeling for binary organic carbonates. J Chem Eng Data 2004;49(2):276–82. http://dx.doi.org/10.1021/je034134e.
[42] Yaws CL, Narasimhan PK. Critical properties and acentric factor—organic compounds. In: Thermophysical properties of chemicals and hydrocarbons. Elsevier; 2009, p. 1–95. http://dx.doi.org/10.1016/B978-081551596-8.50006-7.
[43] Nasirzadeh K, Neueder R, Kunz W. Vapor pressures of propylene carbonate and N, N-dimethylacetamide. J Chem Eng Data 2005;50(1):26–8. http://dx.doi.org/10.1021/je049950g.
[44] Pires J, Timperman L, Jacquemin J, Balducci A, Anouti M. Density, conductivity, viscosity, and excess properties of (pyrrolidinium nitrate-based protic ionic liquid+propylene carbonate) binary mixture. J Chem Thermodyn 2013;59:10–9. http://dx.doi.org/10.1016/j.jct.2012.11.020.
[45] Wagner Z, Bendová M, Rotrekl J. Thermochemical properties of selected terpenes. J Solut Chem 2020;49(9):1137–53. http://dx.doi.org/10.1007/s10953-020-01016-9.
[46] Baird ZS, Uusi-Kyyny P, Pokki J-P, Pedegert E, Alopaeus V. Vapor pressures, densities, and PC-SAFT parameters for 11 bio-compounds. Int J Thermophys 2019;40(11):102. http://dx.doi.org/10.1007/s10765-019-2570-9.
[47] Randová A, Bartovská L, Morávek P, Matějka P, Novotná M, Matějková S, Drioli E, Figoli A, Lanč M, Friess K. A fundamental study of the physicochemical properties of rhodiasolv® polarclean: A promising alternative to common and hazardous solvents. J Mol Liq 2016;224:1163–71. http://dx.doi.org/10.1016/j.molliq.2016.10.085.
[48] Li X, Deng D. Physicochemical property and solubility of SO_2 in glycerin derivatives. J Mol Liq 2018;264:66–71. http://dx.doi.org/10.1016/j.molliq.2018.05.005.
[49] Esteban J, Murasiewicz H, Simons TA, Bakalis S, Fryer PJ. Measuring the density, viscosity, surface tension, and refractive index of binary mixtures of cetane with solketal, a novel fuel additive. Energy Fuels 2016;30(9):7452–9. http://dx.doi.org/10.1021/acs.energyfuels.6b01992.
[50] You X, Chaudhari MI, Pratt LR, Pesika N, Aritakula KM, Rick SW. Interfaces of propylene carbonate. J Chem Phys 2013;138(11). http://dx.doi.org/10.1063/1.4794792.
[51] Zaitseva A, Pokki J-P, Le HQ, Alopaeus V, Sixta H. Vapor–liquid equilibria, excess enthalpy, and density of aqueous γ-valerolactone solutions.. J Chem Eng Data 2016;61(2):881–90. http://dx.doi.org/10.1021/acs.jced.5b00724.
[52] Sharma A, Deepika, Pandey S. Physical properties of renewable solvents cyrene, dimethylisosorbide, γ-valerolactone, cyclopentylmethyl ether, and 2-methyltetrahydrofuran. J Chem Eng Data 2024;69(11):3747–57. http://dx.doi.org/10.1021/acs.jced.4c00259.
[53] Kühn R, Meyer T, Ziegler F. Experimental investigation of ionic liquids as substitute for lithium bromide in water absorption chillers. Energy 2020;205:117990. http://dx.doi.org/10.1016/j.energy.2020.117990.
[54] Fleßner C, Ziegler F. Viscosity correlation for aqueous lithium bromide solution. Int J Thermophys 2023;44(2):21. http://dx.doi.org/10.1007/s10765-022-03122-w.
[55] Mejía A, Herdes C, Müller EA. Force fields for coarse-grained molecular simulations from a corresponding states correlation. Ind Eng Chem Res 2014;53(10):4131–41. http://dx.doi.org/10.1021/ie404247e.
[56] Albà CG, I. AII, Llovell F, F. VL. Assessment of low global warming potential refrigerants for drop-in replacement by connecting their molecular features to their performance. ACS Sustain Chem Eng 2021;9(50):17034–48. http://dx.doi.org/10.1021/acssuschemeng.1c05985.
[57] Paricaud P. Multipolar SAFT-VR mie equation of state: Predictions of phase equilibria in refrigerant systems with no binary interaction parameter. J Phys Chem B 2023;127(13):3052–70. http://dx.doi.org/10.1021/acs.jpcb.3c01058.
[58] Deng D, Han G, Jiang Y, Ai N. Solubilities of carbon dioxide in five biobased solvents. J Chem Eng Data 2015;60(1):104–11. http://dx.doi.org/10.1021/je500812s.
[59] Novak N, Kontogeorgis GM, Castier M, Economou IG. Modeling of gas solubility in aqueous electrolyte solutions with the eSAFT-VR mie equation of state. Ind Eng Chem Res 2021;60(42):15327–42. http://dx.doi.org/10.1021/acs.iecr.1c02923.
[60] Beraldo CS, Liang X, Follegatti-Romero LA. Predicting the solubility of gases in imidazolium-based ionic liquids with SAFT-VR mie EoS by a novel approach based on COSMO. Chem Eng Sci 2024;285:119610. http://dx.doi.org/10.1016/j.ces.2023.119610.
[61] Jovell D, Gómez SB, Zakrzewska ME, Nunes AVM, Araújo JMM, Pereiro AB, Llovell F. Insight on the solubility of R134a in fluorinated ionic liquids and deep eutectic solvents. J Chem Eng Data 2020;65(10):4956–69. http://dx.doi.org/10.1021/acs.jced.0c00588.
[62] Murrieta-Guevara F, Romero-Martinez A, Trejo A. Solubilities of carbon dioxide and hydrogen sulfide in propylene carbonate, N-methylpyrrolidone and sulfolane. Fluid Phase Equilib 1988;44(1):105–15. http://dx.doi.org/10.1016/0378-3812(88)80106-7.
[63] Poggi F, Macchi-Tejeda H, Leducq D, Bontemps A. Refrigerant charge in refrigerating systems and strategies of charge reduction. Int J Refrig 2008;31(3):353–70. http://dx.doi.org/10.1016/j.ijrefrig.2007.05.014.
[64] European Commission. Annex A: Methodology for calculation of GHG emission avoidance. Technical report, Directorate-General for Climate Action, European Commission; 2020.
[65] Gutiérrez-Hernández SV, Rico-Martínez S, Pardo F, Álvarez C, Miguel JA, Zarca G, Urtiaga A. 6FDA-polyimide thin-film composite hollow fiber membranes for hydrofluorocarbons and CO2 separations. J Membr Sci 2024;698:122617. http://dx.doi.org/10.1016/j.memsci.2024.122617.
[66] Asensio-Delgado S, Pardo F, Zarca G, Urtiaga A. Absorption separation of fluorinated refrigerant gases with ionic liquids: Equilibrium, mass transport, and process design. Sep Purif Technol 2021;276:119363. http://dx.doi.org/10.1016/j.seppur.2021.119363.